Journal of Loss Prevention in the Process Industries 105 (2027) 106222



Contents lists available at ScienceDirect

Journal of Loss Prevention in the Process Industries

journal homepage: www.elsevier.com/locate/jlp

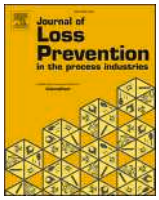

Numerical investigation of obstacle porosity and spatial arrangement in vented dust explosions: Comparison of distributed-porosity rack and pallet configurations

F. Pinna [a,*], M. Zucca [a], M. Simoncelli [b], F. Stochino [a]

[a] Department of Civil and Environmental Engineering and Architecture, University of Cagliari, Via Marengo 2, 09123, Cagliari, Italy
[b] Department of Architecture, Built Environment and Construction Engineering, Politecnico di Milano, Via G. Ponzio 31, 20133, Milano, Italy

ARTICLE INFO

Keywords:
Vented dust explosions
Obstacle porosity
Obstacle spatial arrangement
Flame propagation
Explosion overpressure
Computational fluid dynamics

ABSTRACT

Internal congestion can substantially affect vented dust-explosion loads, yet aggregate porosity does not describe how obstructed regions are spatially distributed. This study investigates the numerical sensitivity of explosion overpressure to obstacle porosity and spatial arrangement using a FLACS-CFD DustEx framework previously calibrated against an unobstructed experimental reference. Fifteen simulations were conducted for a centrally ignited maize-starch cloud in a vented enclosure, comparing an unobstructed configuration with two continuous rack-like and twelve discrete palletized regions of equal gross obstacle volume. Prescribed porosity ranged from 0 to 0.9; at each matched porosity, both layouts had identical fluid-accessible volume and initial dust mass. The unobstructed case produced a maximum monitored overpressure of 0.341 bar(g). At porosities of 0.4–0.9, maximum overpressures ranged from 0.325 to 0.493 bar(g) for racks and from 0.451 to 0.586 bar(g) for pallets, with pallet values 18.9–38.8% higher at equal porosity. In contrast, for fully impermeable regions, the rack and pallet predictions were 0.383 and 0.252 bar(g), respectively. The rack–pallet ordering was consistent across maximum overpressure and maximum positive pressure-rise rate but reversed between impermeable and partially porous cases. Published experimental benchmarks support the FLACS/PDR methodology for selected obstructed gas-explosion conditions, while dust-explosion studies provide complementary evidence for the combustion modelling framework. The present application, based on idealized rack and pallet volumes with prescribed equal area and volume porosities, is methodologically supported but has not been directly validated against corresponding physical storage configurations. Accordingly, the calculated pressure differences represent internally consistent, model-dependent trends rather than experimentally confirmed severity rankings.

1. Introduction

Combustible dust explosions represent a persistent hazard in industries involving the production, handling, transport and storage of particulate solids. Food processing, agriculture, woodworking, pharmaceutical manufacturing, chemical production and metal processing are among the sectors in which suspended dust clouds may ignite and generate rapid pressure rises, severe structural damage and secondary explosions (Huang et al., 2025; Su et al., 2025; Wang et al., 2025, 2026; Jung et al., 2026). Structural failure may also generate high-velocity fragments, creating an additional impact hazard for nearby equipment and personnel; the effects of blast-induced fragments and the protective performance of cellular materials have been investigated experimentally by Ranwaha and Yuen (2016). The consequences may extend beyond the initially affected equipment, as the primary event can disperse deposited dust, propagate flames through connected units and initiate further explosions, including through ducts and interconnected process equipment (Skjold et al., 2026). Accordingly, dust explosion prevention and mitigation remain central components of industrial process-safety management (Abbasi and Abbasi, 2007; Yuan et al., 2015; Pinna et al., 2025). The long-term persistence of this hazard is illustrated in Fig. 1, which presents the average annual number of reported dust explosions across selected historical and recent periods.

The historical compilation developed by Yuan et al. (2015) shows

* Corresponding author.
E-mail addresses: francesco.pinna4@unica.it (F. Pinna), marco.zucca2@unica.it (M. Zucca), marco.simoncelli@polimi.it (M. Simoncelli), fstochino@unica.it (F. Stochino).

https://doi.org/10.1016/j.jlp.2026.106222
Received 3 August 2026; Received in revised form 13 October 2026; Accepted 26 October 2026
Available online 28 October 2026
0950-4230/© 2026 The Authors. Published by Elsevier Ltd. This is an open access article under the CC BY license (http://creativecommons.org/licenses/by/4.0/).

substantial variations in the reported occurrence of dust explosions between 1930 and 2012, with the highest average values observed during the 1960–1980 period. More recent worldwide records compiled by Pinna et al. (2025) indicate an average of 57.8 reported explosions per year between 2016 and 2023, confirming that dust explosions remain a recurrent industrial safety concern. However, the apparent difference between the historical and recent values should not be interpreted as direct evidence of an increase in the actual occurrence frequency, as the higher recent values may partly reflect improved data availability and reporting coverage. Nevertheless, the available evidence demonstrates that dust explosions remain a significant global process-safety concern.

Explosion venting is one of the most widely adopted protection measures for enclosures that cannot be designed to withstand the maximum pressure of an unvented deflagration. A vent provides a controlled flow path for unburned mixture and combustion products, thereby limiting the pressure developed inside the protected enclosure. The reduced explosion pressure, P_{red}, depends on the dust explosibility properties, vent area, enclosure volume and geometry, static activation pressure, ignition conditions and characteristics of the initial dust cloud. Recent dimensional-analysis approaches have further demonstrated that dust-explosion severity results from the combined influence of particle size, dust concentration, interparticle spacing, chamber characteristic length, and the physical and chemical properties of the combustible material. Generalized correlations based on dimensionless parameters have consequently been proposed for predicting maximum explosion pressure and rate of pressure rise under varying conditions (Alauddin et al., 2026). These effects form the basis of established design methods (National Fire Protection Association, 2023) (European Committee for Standardization, 2012). Nevertheless, vent-sizing relations are necessarily simplified representations of a highly transient multiphase combustion process and may not fully capture the behaviour of non-standard or internally congested equipment (Tamanini and Valiulis, 1996; Tamanini, 1998; Zalosh, 2007; Pinna et al., 2025, 2026a).

Turbulence is one of the most influential parameters governing dust flame propagation. It affects dust dispersion, particle–oxidizer mixing, flame wrinkling and the effective burning rate. Large-scale experiments conducted by Tamanini (1998) demonstrated that the pressure generated during vented dust explosions is strongly dependent on the turbulence level at ignition. This evidence subsequently supported the introduction of specific provisions for turbulent operating conditions in venting guidance (Zalosh, 2007). Turbulence during an industrial explosion is not limited to the initial state of the dust cloud. Additional turbulence is generated after ignition by the expansion-induced flow and by its interaction with walls, internal equipment and geometric discontinuities. Therefore, the internal configuration of an enclosure may affect the explosion even when the dust properties, concentration, vent and ignition source remain unchanged.

The influence of obstacles on flame acceleration has been extensively investigated for gaseous deflagrations. Obstacles modify the flow field, generate shear layers and recirculation regions, increase the flame surface area and may introduce additional pressure peaks. Experimental and numerical investigations have shown that blockage ratio, obstacle size, shape, spacing, position and arrangement can all affect flame propagation and explosion overpressure (Li et al., 2016; Wang et al., 2022; Mahesh et al., 2025). Configurations characterized by the same overall blockage may not produce the same response when the obstructed volume is distributed differently. However, obstacles do not act solely as turbulence generators. They also displace combustible mixture, restrict available propagation paths, produce shielding effects and modify the interaction between the internal combustion process and the vent discharge. Their net influence may therefore be amplified, approximately neutral or mitigating, depending on the specific configuration.

Compared with gaseous explosions, the controlled assessment of obstacle effects in vented dust explosions remains less developed. Dust explosions involve additional processes associated with particle dispersion, heating, devolatilization, heterogeneous combustion, agglomeration and settling, making the relationship between turbulence and flame propagation particularly complex. Previous computational studies have examined the influence of vent dimensions, vent activation pressure, vent-panel inertia, ignition position, dust-cloud size, concentration and enclosure geometry. FLACS-CFD DustEx, the dust-explosion modelling framework implemented within the FLACS-CFD

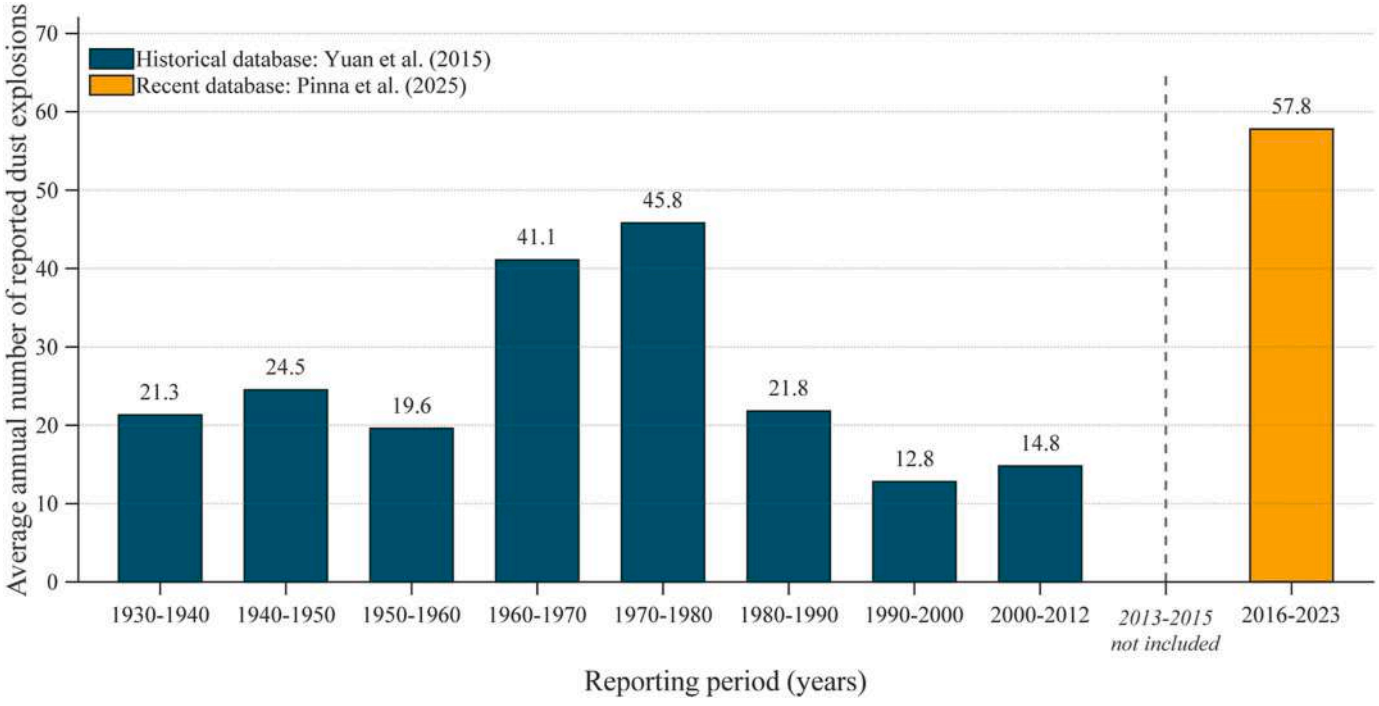

Fig. 1. Average annual number of reported dust explosions across selected historical and recent periods. Historical data for 1930–2012 were derived from Yuan et al. (2015), whereas the 2016–2023 value was obtained from the worldwide incident database compiled by Pinna et al. (2025). Data for 2013–2015 were not included.

computational fluid dynamics software developed by Gexcon, has been applied to the simulation of vented dust explosions in vessels and silos. Previous studies have reported comparisons with experimental pressure histories, while alternative Reynolds-averaged Navier–Stokes models have also achieved good agreement for vented corn-starch explosions (Tascón and Aguado, 2015, 2017; Huang et al., 2022; Varela et al., 2023). These studies demonstrate the potential of validated and calibrated computational fluid dynamics models to investigate conditions that are difficult or costly to reproduce through extensive large-scale testing.

The importance of internal congestion is particularly evident in industrial equipment containing filter elements, shelves, storage structures or process components. Recent studies on baghouse dust collectors have shown that their obstacle-rich internal geometry may produce reduced explosion pressures that differ substantially from predictions derived for nominally empty vessels. Collector-specific analyses have therefore introduced congestion measures based on the internal filter volume and highlighted the need to account for the physical organization of the equipment when evaluating explosion loads (Pinna et al., 2025, 2026a, 2026b). These developments confirm that internal obstacles cannot always be represented adequately by the external enclosure volume alone. Nevertheless, aggregate congestion parameters, such as total obstructed volume or average blockage, do not explicitly distinguish between a continuous obstacle region and the same volume divided into several separate elements. Despite the recognized role of turbulence and congestion, the literature reviewed here does not appear to provide a systematic comparison of continuous and discrete storage layouts in a vented dust explosion while maintaining the same enclosure, vent, dust cloud, ignition conditions, gross obstacle volume and nominal porosity. Most investigations vary several geometric parameters simultaneously, making it difficult to isolate the influence of obstacle spatial arrangement. Consequently, it remains unclear whether configurations characterized by the same occupied volume and porosity can be considered equivalent for dust explosion hazard assessment. This issue is particularly relevant to industrial storage environments, where the same quantity of material or equipment may be arranged as continuous rack-like structures or distributed among multiple palletized units. To address this gap, the present study investigates the combined influence of obstacle porosity and spatial arrangement using a previously calibrated FLACS-CFD DustEx modelling framework. Fifteen simulations are performed by comparing an unobstructed reference enclosure with continuous rack-like and discrete pallet-like configurations having the same gross occupied volume. The rack and pallet configurations were represented by idealized macroscopic volumes using the standard FLACS-CFD geometry and porosity inputs. Equal values of area and volume porosity were prescribed for each investigated condition, without explicitly resolving individual rack or pallet components. Pressure histories, peak monitored overpressures, temperature fields and combustion-product distributions are analyzed to determine whether porosity alone is sufficient to characterize internal congestion. Following this introduction, Section 2 describes the experimental setup adopted as the reference configuration. Section 3 presents the assessment of the numerical framework against the experimental results. Section 4 outlines the numerical modelling strategy and analyses the effects of obstacle arrangement and porosity. The main findings are discussed in Section 5, while Section 6 summarizes the conclusions of the study.

2. Experimental reference configuration

The experimental campaign used as the reference for the numerical model developed in the present study was conducted by Tamanini (1990) at the Factory Mutual Research Corporation (FMRC). The tests were designed to investigate the influence of background turbulence on vented dust explosion severity. Different turbulence levels were obtained by varying the delay between dust injection and ignition, thereby exploiting the natural decay of the velocity field generated by the pneumatic dispersion system. A schematic representation of the FMRC experimental chamber is shown in Fig. 2. Internal obstacles were not present in the original experiments. The principal characteristics of the facility are summarized in Table 1.

The dust was introduced through a canister located downstream of each compressed-air tank. Activation of the quick-opening valves caused the compressed air to entrain the dust and inject it through all sixteen nozzles. The valve activation required approximately 50 ms, followed by approximately 100 ms for pressurization of the dust canister. Most cornstarch tests employed a centrally positioned 5 kJ chemical ignitor, whereas the coal tests generally used a 50 g black-powder charge. A jet-flame ignition arrangement was also examined in two tests. The main test conditions are summarized in Table 2.

The velocity field generated by the pneumatic dust-injection system was characterized at multiple locations within the chamber. The measurements revealed a strongly non-uniform, time-dependent flow dominated by large-scale motion. The root-mean-square instantaneous velocity was therefore adopted as the representative turbulence parameter. Additional measurements performed in the presence of cornstarch showed that the dust prolonged the transient injection. Empirical decay relationships were subsequently derived and used by Tamanini to estimate the turbulence level corresponding to each ignition delay. The experimental results indicated that explosion severity increased with increasing turbulence intensity.

3. Numerical model and assessment

The experimental configuration described in Section 2 was reproduced using FLACS-CFD DustEx 24.2. The numerical model represented the unobstructed FMRC chamber and was developed with reference to the cornstarch experiment performed with the full vent opening, a centrally positioned chemical ignitor, a nominal dust concentration of 0.250 kg m^{-3}, and an ignition delay of approximately 0.50 s.

Tamanini (1990) measured the chamber pressure using two transducers mounted on the side walls, although their exact coordinates were not reported. For the present assessment, the numerical pressure history was extracted at $(x, y, z) = (4.55, 1.20, 1.50)$ m, which is in the fluid region 0.05 m from one of the chamber side walls and at mid-height. This location was adopted as a representative wall-adjacent pressure-monitoring point rather than as an exact reproduction of the experimental transducer position. The experimental pressure transducers and the pneumatic injection system were both installed on the chamber side walls.

The pressure quantity considered in the present study corresponds to the chamber static gauge overpressure relative to the initial ambient pressure, consistently with the pressure measurements reported by Tamanini (1990). Dynamic and total pressure quantities were not considered. The term reduced explosion pressure, P_{red}, is retained when referring to the maximum chamber overpressure conventionally used in vented-explosion assessment.

The pneumatic dust-dispersion phase was not simulated explicitly. Instead, the numerical calculation was initialized at ignition by prescribing a homogeneous dust cloud and a background turbulence level representative of the experimental conditions at that instant. This approach avoided the explicit modelling of the compressed-air tanks, dust canisters, piping and injection nozzles, while retaining the main influence of the dispersion process on the subsequent flame development and pressure rise.

The simulations were performed using the three-dimensional transient compressible formulation implemented in FLACS-CFD DustEx. The solver is based on the Reynolds-averaged conservation equations for mass, momentum, energy and transported scalar quantities on a Cartesian finite-volume grid. The effect of geometrical blockage at the computational-cell level is incorporated through the FLACS area- and

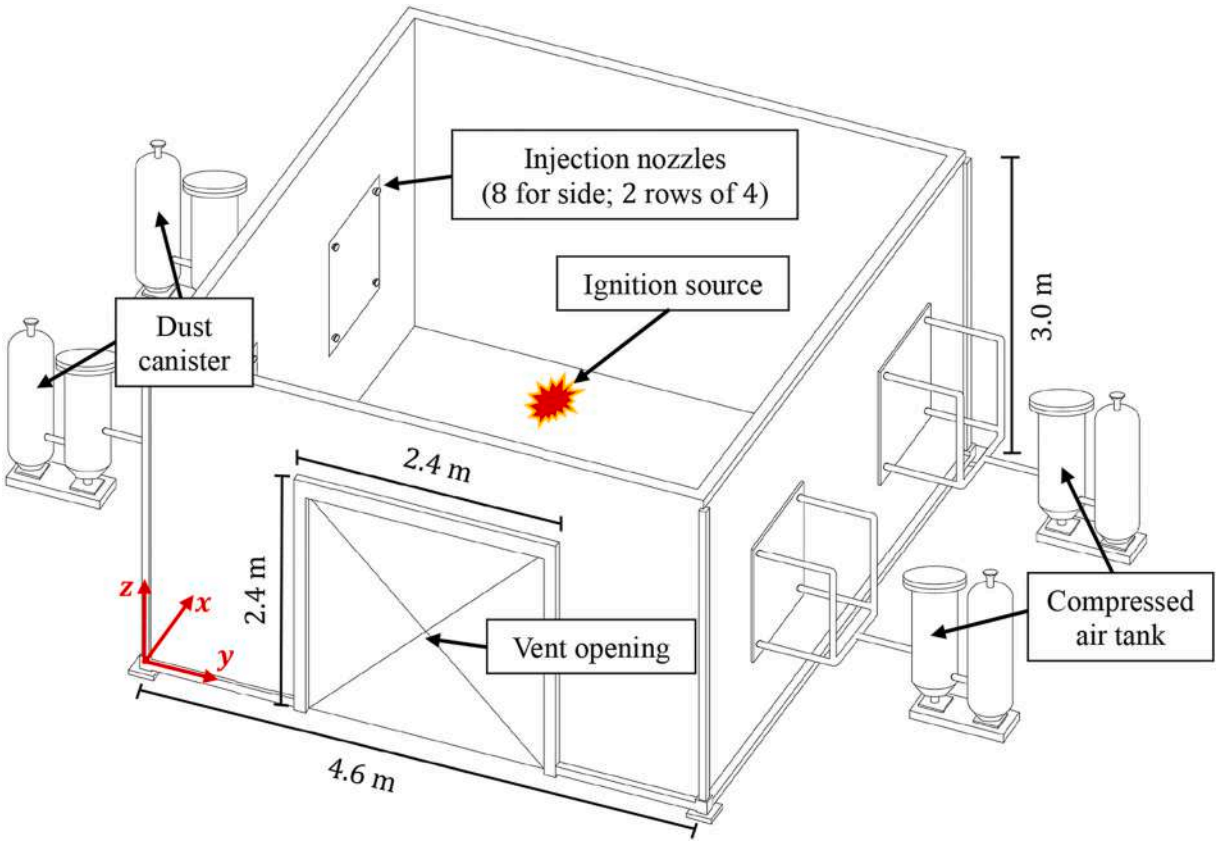

Fig. 2. Redrawn schematic of the FMRC large-scale vented dust explosion facility described by Tamanini (1990), showing the chamber geometry, vent opening, pneumatic dust-dispersion system and central ignition position.

Table 1
Main characteristics of the FMRC experimental facility and measurement system, based on Tamanini (1990).

Parameter	Description
Chamber dimensions	4.6 × 4.6 × 3.0 m
Nominal chamber volume	63.7 m^3
Chamber construction	32 mm steel-faced plywood panels supported by a steel frame
Design pressure	0.69 bar(g)
Main vent opening	2.4 × 2.4 m located on one vertical wall
Vent condition	Uncovered opening; no vent-panel inertia or static opening pressure
Pressure-transducer range	0 – 207 kPa(abs)
Compressed-air tanks	Four tanks, each with a volume of 0.33 m^3
Initial tank pressure	8.3 bar(g)
Final tank pressure	Approximately 1.4 bar(g)
Injection nozzles	Sixteen nozzles mounted on two opposite walls
Nozzle arrangement	Eight nozzles per wall, arranged in two rows of four
Nozzle geometry	51 mm end cap with twelve 11 mm holes
Hole orientation	Four holes at 20 ° and eight at 50 °
Velocity probe	Fast-response bidirectional impact probe
Frequency response	Approximately 400 – 500 Hz
Estimated velocity accuracy	10 – 20%
Velocity noise threshold	Approximately 2.5 m s^{-1}
Acquisition frequency	2000 scans/s for velocity measurements; 500 scans/s during explosion tests

Table 2
Dust properties and principal conditions of the vented explosion campaign, based on Tamanini (1990).

Parameter	Cornstarch	Bituminous-coal mixture
Number of tests	11	10
Nominal concentration	250 g m^{-3}	250 g m^{-3}
Additional concentration	One test at 500 g m^{-3}	—
Moisture content	Approximately 10%	4.3%
Mass-mean particle diameter	15 μm	—
Particle-size distribution	99.5% below 25 μm; 15 % below 5 μm	50% below 150 μm; 27 % below 75 μm; 7.8 % below 45 μm
Main ignition source	5000 J chemical ignitor	50 g black powder
Nominal ignition delay	500 – 1300 ms	500 – 900 ms
Reported peak pressure	Approximately 0.14 – 0.43 bar(g)	Up to approximately 0.35 bar(g)

volume-porosity formulation. The governing equations, including the area- and volume-porosity formulation, the treatment of obstacle resistance and the turbulence transport models, are documented in the technical reference material included in the FLACS-CFD 24.2 User's Manual (Gexcon AS, 2025).

Turbulent transport was represented using the K-EPS-1 model available in FLACS-CFD DustEx (Lyu et al., 2024). Dust combustion was described using the BETA3 model. The FLACS-CFD DustEx combustion framework represents turbulent flame propagation through an engineering-scale burning-velocity formulation; its development and application to dust clouds, including maize starch, are discussed in detail by Skjold et al. (2014). Applications of the same FLACS-CFD DustEx framework to vented maize-starch explosions can also be found in Tascón and Aguado (2017). No modification to the governing flow, turbulence or combustion equations implemented in FLACS-CFD DustEx was introduced in the present study.

The numerical control parameters CFLC and CFLV were set to 5 and 0.5, respectively (Gexcon AS, 2025).

The chamber and vent geometries were reproduced according to the experimental configuration presented in Section 2. The enclosure walls were modelled as solid and impermeable boundaries, while the wall opening was represented as a permanently open vent. The additional roof vents present in the experimental facility were excluded because they were not used in the selected experiment.

An external region was included around the enclosure, particularly downstream of the vent, to permit the discharge of the pressure wave, unburned mixture and combustion products without immediate interaction with the computational boundaries. The domain extended from −5.0 to 10.0 m in the *x*-direction, from −0.1 to 10.1 m in the *y*-direction, and from −0.2 to 5.5 m in the vertical direction. A preliminary grid-sensitivity assessment was performed for the unobstructed reference configuration before defining the computational mesh adopted for parametric investigation. In addition to the selected uniform cell size of 0.05 m, a refined grid with a uniform cell size of 0.025 m was considered while maintaining the same computational domain, physical initial conditions, ignition parameters, dust properties and numerical settings. Refining the grid from 0.05 m to 0.025 m resulted in a variation of 1.98% in the maximum monitored overpressure. The finer grid, however, produced a substantial increase in the number of computational cells and consequently in the computational cost. Considering the limited variation in the principal pressure metric, the markedly higher computational demand of the 0.025 m grid, and the FLACS-CFD grid recommendations, the 0.05 m resolution was therefore selected for parametric investigation. The same mesh was retained for all rack and pallet simulations to ensure a consistent numerical discretization throughout the comparative analysis (Gexcon AS, 2025). The resulting grid contained $300 \times 204 \times 114$ cells, corresponding to 6,976,800 control volumes. The same computational domain and nominal mesh resolution were retained for all simulations involving internal obstacles, ensuring consistent grid spacing across the investigated configurations. Nevertheless, this approach does not eliminate possible configuration-dependent discretization errors arising from the different spatial distributions and cell-level representations of the obstacle regions. The initial absolute pressure and temperature were set to 1 bar and 293.15 K, respectively. A localized ignition source with an energy of 5.0 kJ was positioned at the geometrical center of the enclosure.

The distributed-porosity representation adopted in FLACS-CFD is not specific to the DustEx combustion model but forms part of the general porosity/distributed-resistance (PDR) treatment used to represent geometrical blockage and sub-grid obstacles. Previous validation studies of FLACS for vented gaseous deflagrations have included internally obstructed configurations and have compared calculated pressure responses with experimental measurements. Vyazmina and Jallais (2016), for example, assessed FLACS against vented hydrogen-explosion experiments including internal obstacles, while Lucas et al. (2021) evaluated the PDR-based FLACS framework against vented deflagration experiments in obstructed 20-ft containers. These studies provide independent support for the capability of the FLACS PDR approach to represent the global influence of congestion on flow development and explosion overpressure. However, they do not constitute a direct validation of the specific homogeneous rack and pallet representations adopted in the present dust-explosion simulations. The comparison with Tamanini (1990) demonstrates agreement between the calibrated DustEx model and the selected unobstructed experimental reference. However, because the same experimental case was used to calibrate the combustion reactivity parameter, this comparison does not constitute independent validation. The subsequent rack and pallet results should therefore be interpreted as comparative numerical responses within the adopted distributed-porosity framework rather than as quantitatively validated predictions of actual storage systems.

3.1. Initial dust-cloud and turbulence conditions

The chamber was initially filled with a homogeneous maize-starch cloud having a concentration of 250 g m^{-3}. Since the numerical simulation started directly at ignition, the preceding pneumatic dust-dispersion process was not simulated explicitly. Its influence on the flow field at the ignition instant was instead represented through the prescribed initial turbulence conditions.

Tamanini (1990) characterized the temporal evolution of the velocity field generated by the pneumatic dust-dispersion system in the FMRC chamber. Because the measured flow was strongly non-uniform and characterized by significant large-scale motion, three quantities were evaluated: the mean velocity, the root-mean-square (RMS) of the fluctuating velocity component, and the RMS of the instantaneous velocity. Tamanini selected the latter as the most appropriate parameter for characterizing the turbulence conditions in the chamber. Accordingly, U_{rms} used herein denotes the root-mean-square of the instantaneous velocity, and not the RMS of the fluctuating component.

For the experiments involving cornstarch at a nominal concentration of 250 g m^{-3}, velocity measurements obtained at two locations near the chamber center were converted into representative chamber-averaged values using the experimentally determined scaling factor of 0.72 reported by Tamanini (1990). The resulting chamber-averaged RMS instantaneous velocity was described by the following empirical correlations: $U_{rms} = 20.04 - 12.95t$, $0.25 \le t \le 0.984\ s$ and $U_{rms} = 6.95t^{-3.07}$, $t > 0.984\ s$. Where U_{rms} is expressed in m s^{-1} and t denotes the time elapsed from the beginning of dust injection. These relationships were derived by Tamanini (1990) specifically from the turbulence measurements performed in the FMRC chamber and were subsequently used to estimate the turbulence conditions corresponding to the different ignition times of the vented dust-explosion tests.

For the nominal ignition delay of $t = 0.50$ s adopted in the reference experiment, the first correlation gives $U_{rms} = 20.04 - 12.95(0.50) = 13.57$ m s^{-1}.

This value defines the experimental turbulence condition that the numerical initialization was intended to reproduce. In FLACS-CFD DustEx, the initial turbulence condition was prescribed using a characteristic velocity of 20 m s^{-1} together with a turbulence intensity of 0.68. The characteristic velocity should therefore not be interpreted as a directly measured chamber velocity. Rather, the combination of these two input parameters yielded an initial turbulent velocity of $20{\cdot}0.68 = 13.6$ m s^{-1}, which closely reproduces the $U_{\mathrm{rms}} = 13.57$ m s^{-1} estimated from the Tamanini (1990) correlation at the ignition instant. The value of 20 m s^{-1} was therefore selected together with the prescribed turbulence intensity to reproduce the experimentally estimated turbulence condition, rather than as an independently measured velocity quantity.

A turbulent length scale of 0.025 m was also prescribed. Since the numerical calculation was initialized directly at ignition, these parameters represent the turbulence state inherited from the preceding pneumatic dispersion process at that instant. The subsequent evolution of turbulence, combustion, flame propagation, pressure development and vent discharge was then calculated directly by the numerical solver without further adjustment of the initial turbulence parameters.

3.2. Calibration of the maize-starch combustion model

The cornstarch employed in the experimental campaign was not directly available as a corresponding fuel definition within FLACS-CFD DustEx. A dedicated numerical fuel model was therefore developed to reproduce, as closely as possible, the characteristics reported by Tamanini (1990). The custom fuel files were derived from a common maize-starch formulation and incorporated the available experimental particle properties, including the representative particle diameter and particle density reported for the experimental dust.

The combustion model implemented in FLACS-CFD DustEx

originates from the modelling approach developed within DESC, in which turbulent flame propagation in dust clouds is described through an engineering-scale combustion formulation based on turbulent burning-velocity concepts. The applicability of this framework to maize-starch explosions and its comparison with experimental flame-propagation and pressure data were investigated by Skjold et al. (2014). More specifically for vented dust explosions, Tascón and Aguado (2017) applied FLACS-CFD DustEx to maize-starch experiments in a 5.2 m^3 vessel and demonstrated through a sensitivity analysis that the calculated pressure response depends appreciably on both dust-air mixture reactivity and computational grid resolution.

In the present study, the dust concentration, particle properties, thermochemical properties, nominal deflagration index and maximum explosion pressure were maintained unchanged. A controlled sensitivity analysis was instead performed on the FLACS-CFD DustEx reactivity correction factor, C_L, which was varied to modify the numerical reactivity assigned to the common maize-starch combustion model. Four custom fuel files were generated using C_L values of 1.25, 1.50, 1.75 and 2.00. These files are identified in Fig. 3 as MAIZE 125, MAIZE 150, MAIZE 175 and MAIZE 200, respectively. The four cases therefore do not represent different dust materials, concentrations or explosibility classes; rather, they represent progressively increasing numerical reactivity levels applied to the same maize-starch formulation for the purpose of assessing the sensitivity of the predicted pressure response and selecting the parameterization that best reproduced the experimental reference case.

All other numerical inputs were kept unchanged during this calibration process, including the particle properties, dust concentration, chamber and vent geometry, computational mesh, ignition energy, initial turbulence conditions and solver parameters. The resulting differences in the calculated pressure histories can therefore be attributed exclusively to the prescribed reactivity level.

Fig. 3 compares the experimental static overpressure history with the numerical predictions obtained using the four custom fuel files. Since the experimental time was referenced to the beginning of the pneumatic dust-injection process, whereas the numerical calculations started directly at ignition, the numerical histories were translated rigidly along the time axis to align their principal peaks with the experimental maximum. No scaling or modification of the pressure amplitudes was applied.

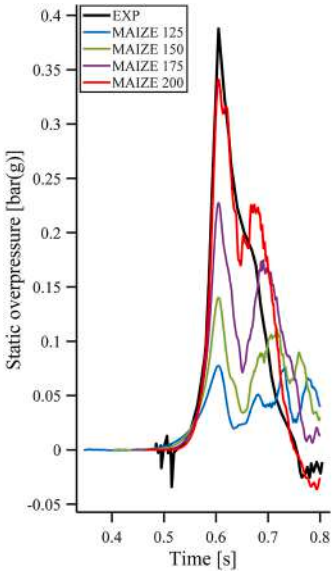

Fig. 3. Comparison between the experimental static-overpressure history and the FLACS-CFD DustEx predictions obtained using four custom maize-starch parameterizations with progressively increasing reactivity.

The predicted pressure response increased progressively with increasing C_L. The $C_L = 1.25$ and $C_L = 1.50$ cases substantially underestimated both the pressure-rise rate and the experimental maximum, while $C_L = 1.75$ provided a closer response but still underestimated the measured peak. The $C_L = 2.00$ case provided the closest agreement with the experimental pressure-rise phase and peak magnitude. Accordingly, $C_L = 2.00$ was selected for the calibrated maize-starch model and was subsequently maintained unchanged in all simulations included in the obstacle-porosity investigation. This calibration was therefore performed only once against the unobstructed experimental reference configuration and was not adjusted separately for the rack or pallet cases.

The selected reactivity correction factor should therefore be regarded as a calibration parameter associated with the unobstructed reference configuration rather than as an independently validated parameter for internally congested conditions. Maintaining the same value in all subsequent simulations avoided case-specific re-tuning and ensured a consistent combustion parameterization throughout the comparative analysis. However, this procedure does not demonstrate that the calibrated combustion response remains quantitatively predictive when internal obstacles are introduced. The transferability of the calibrated parameterization to congested configurations therefore represents an additional limitation of the present study. The main properties of the selected dust model are summarized in Table 3.

3.3. Assessment of the calibrated model

The final assessment was performed using the selected MAIZE 200 parameterization. The assessment considered both the static overpressure history and the cumulative positive-pressure impulse, thereby assessing the ability of the model to reproduce both the maximum pressure and the overall pressure–time loading.

Fig. 4(a) compares experimental and numerical static overpressure histories. The numerical model reproduced the rapid initial pressure rise, the occurrence of the main pressure peak, and the overall duration of the positive-pressure phase. The experimental maximum static overpressure was approximately 0.390 bar(g), whereas the numerical simulation produced a maximum monitored overpressure of approximately 0.341 bar(g). The model therefore underestimated the experimental peak by approximately 12%.

Differences were more evident during the post-peak phase, particularly in the secondary pressure fluctuations. The numerical curve exhibited a more pronounced secondary peak and a slightly different pressure-decay profile. These discrepancies may be attributed to the homogeneous initialization of the dust cloud, the omission of the pneumatic dispersion process, and the use of a predefined numerical fuel formulation rather than the exact cornstarch employed in the experiment.

The cumulative positive-pressure impulse was calculated as:

$$I_p(t) = \int_{t_0}^{t} \max[P_{red}(\tau), 0] d\tau \quad (1)$$

Table 3
Dust-cloud and turbulence parameters adopted in the selected numerical model.

Parameter	Numerical setting
Dust material	Maize starch
Dust concentration	0.250 kg m^{-3}
Maximum unvented explosion pressure	8.6 bar(g)
Deflagration index	150 bar(g) m s^{-1}
Particle density	1180 kg m^{-3}
Representative particle diameter	15 μm
Characteristic velocity	20 m s^{-1}
Turbulence intensity	0.68
Initial turbulent velocity	13.6 m s^{-1}
Turbulent length scale	0.025 m

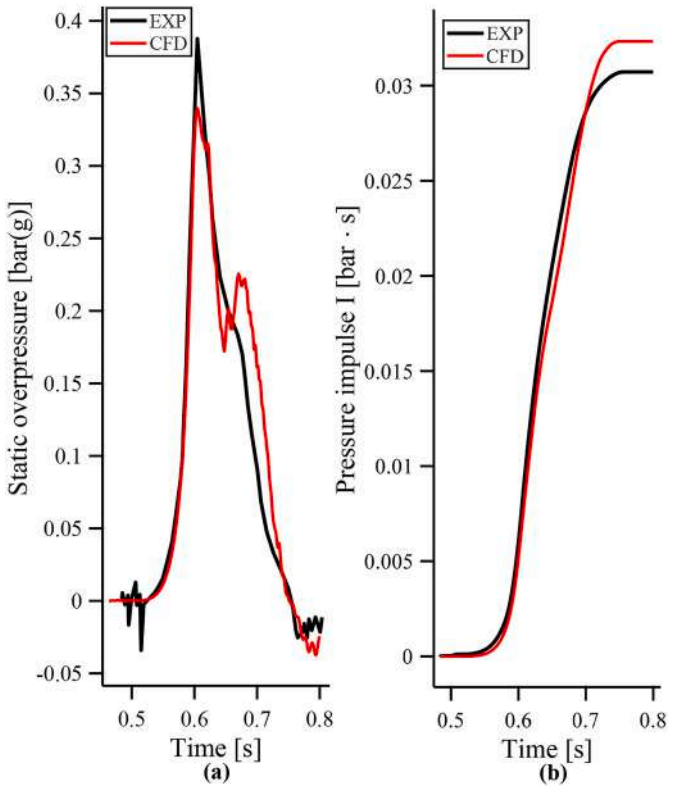

Fig. 4. Final assessment of the selected MAIZE 200 numerical model against the experimental results: (a) comparison of the static overpressure histories and (b) comparison of the corresponding cumulative positive-overpressure impulses.

where t_0 denotes the beginning of the positive-pressure phase.

As shown in Fig. 4(b), the numerical and experimental impulse histories exhibited very similar developments. The experimental final impulse was approximately 0.031 bar(g) s, whereas the numerical simulation produced approximately 0.032 bar(g) s. The difference in final cumulative impulse was therefore approximately 5%, despite the moderate underprediction of the pressure peak.

The dust properties, initial turbulence conditions, ignition energy and position, computational domain, mesh, monitoring locations, and numerical control parameters were maintained unchanged. The calibrated combustion parameterization and all numerical-model parameters were retained unchanged in the subsequent obstacle simulations. Consequently, the calculated differences represent the response of the same numerical framework to the prescribed obstacle configurations, rather than differences introduced through case-specific recalibration. This consistency is important for comparative analysis but should not be interpreted as independent validation of the model for congested conditions.

3.4. *Independent benchmark-based assessment of the distributed-porosity approach*

The experimental assessment presented in Section 3.3 concerns the unobstructed reference enclosure and therefore does not directly establish the predictive accuracy of FLACS-CFD DustEx for internally congested configurations. To further examine the applicability and transferability of the adopted distributed-porosity representation, an additional assessment was conducted using published experimental benchmarks and independent numerical investigations involving obstructed explosion configurations. This assessment focuses on three complementary aspects: (i) the ability of FLACS to reproduce experimentally observed congestion effects in vented gaseous deflagrations, (ii) the experimental evidence supporting DESC/FLACS-DustEx for dust explosions involving geometric complexity and internal obstacles, and (iii) independent evidence concerning the influence of obstacle spatial arrangement at comparable blockage conditions.

The porosity/distributed-resistance (PDR) formulation implemented in FLACS accounts for the effects of unresolved geometric obstructions through area and volume porosity, together with sub-grid resistance and turbulence-generation contributions. Its application to congested industrial environments has been investigated through comparisons with experimental deflagration data involving different obstacle arrangements and blockage levels (Hansen et al., 2005; Pedersen and Middha, 2012; Ma et al., 2014; Vyazmina and Jallais, 2016; Diakow et al., 2018; Lucas et al., 2021).

Pedersen and Middha (2012) investigated vented propane–air explosions in an approximately 64 m^3 enclosure, considering configurations with and without eight internal obstacles. The comparison showed that FLACS reproduced several pressure-generation mechanisms associated with obstacle-induced flame acceleration, with reasonable agreement for selected pressure peaks. However, discrepancies remained for pressure oscillations dominated by acoustic effects. This study is particularly relevant because it provides experimental evidence for the treatment of obstruction effects in a vented enclosure of a scale comparable to that adopted in the present investigation.

Further quantitative evidence is provided by Diakow et al. (2018), who compared large-scale vented propane–air deflagration experiments with FLACS simulations for three congestion levels. Additional hydrogen–air benchmarks were reported by Vyazmina and Jallais (2015), including configurations with and without eight obstacles. Representative experimental and numerical overpressures from these investigations are summarized in Table 4.

Vyazmina and Jallais (2015) also identified limitations associated with the sub-grid representation of obstacles. They reported that the porosity-based treatment could overestimate turbulence generation, flame propagation velocity and the resulting overpressure, recommending the explicit on-grid representation of obstacles under conditions of relatively limited congestion. This observation is particularly relevant to the present investigation, since the adopted rack and pallet regions are prescribed through uniform porosity values rather than reconstructed from detailed obstacle geometries.

The results demonstrate that FLACS can reproduce the direction of experimentally observed changes associated with congestion, although

Table 4
Representative experimental benchmarks for FLACS predictions in obstructed vented gas explosions.

Reference	Configuration	EXP [bar (g)]	FLACS [bar(g)]	Error
Vyazmina and Jallais (2015)	H_2–air, unobstructed	0.150	0.180	+20.0%
Vyazmina and Jallais (2015)	H_2–air, 8 obstacles	0.430	0.690	+60.5%
Diakow et al. (2018)	Propane–air, ABR = 11%	0.372	0.965	+159.3%
Diakow et al. (2018)	Propane–air, ABR = 7.6%	0.269	0.634	+135.9%
Diakow et al. (2018)	Propane–air, ABR = 4.2%	0.138	0.269	+95.0%

Note: Error is calculated as $100(P_{FLACS} - P_{EXP})/P_{EXP}$. Values from Diakow et al. (2018) are series-averaged peak pressures converted from psig to bar(g); errors were calculated from the originally reported pressure values in psig, before conversion and rounding to bar(g). The hydrogen cases have slightly different initial concentrations and should not be interpreted as a strictly isolated variation of obstruction alone. The benchmarks involve different fuels, numerical versions and experimental configurations and are not pooled into a single validation statistic.

appreciable discrepancies may occur in absolute peak overpressure. In the experiments reported by Diakow et al. (2018), reducing the area blockage ratio from 11% to 4.2% decreased the measured peak pressure from 5.4 to 2.0 psig, while FLACS predicted a corresponding decrease from 14.0 to 3.9 psig. Thus, the model reproduced the experimental ordering of the congestion levels, while overestimating the magnitude of the pressures. Similarly, the hydrogen benchmarks reported by Vyazmina and Jallais (2015) showed increased overpressure in the presence of obstacles, with a more pronounced numerical prediction than that observed experimentally. These comparisons indicate that reproducing a congestion-related trend does not necessarily imply quantitative accuracy.

For combustible dusts, Skjold et al. (2014) investigated maize-starch explosions in a 3.6 m flame-acceleration tube, including configurations with 10 and 20 internal obstacles, and compared the experimental response with DESC simulations. The numerical predictions showed reasonable agreement with selected experimental pressure histories, supporting the applicability of the DESC combustion framework to obstacle-influenced dust-flame propagation. Nevertheless, the experiments exhibited substantial variability, and the test conditions were not identical across all configurations.

Additional experimental assessments of DESC/FLACS-DustEx have been reported for vented dust explosions in silos and vessels (Skjold et al., 2006; Castellanos et al., 2013; Tascón and Aguado, 2017). These studies provide evidence for the capability of the dust-explosion framework to reproduce selected pressure responses and the influence of venting conditions, while also identifying sensitivity to combustion parameters, numerical resolution and geometrical details. They do not, however, directly validate the homogeneous porous obstacle regions considered in the present study.

The broader applicability of the PDR methodology has also been examined using independent numerical implementations. Puttock et al. (2022) validated the PDRFoam model against more than 150 gas-explosion experiments involving variations in blockage ratio, obstacle size, shape, spacing and configuration. The simulations reproduced several experimentally observed trends, with predicted maximum overpressures generally within a factor of two of the measurements. Dhiman et al. (2023) further assessed PDRFoam against experimental explosion benchmarks, providing additional evidence for the applicability of the PDR concept while highlighting the influence of mesh resolution and obstacle representation. Although these results support the broader modelling methodology, differences in solver formulation and sub-grid parameterization prevent their interpretation as a direct validation of FLACS-CFD DustEx.

Of relevance to the influence of spatial arrangement, Mahesh et al. (2025) performed geometrically resolved large-eddy simulations of vented methane–air explosions considering four obstacle configurations with identical volume and area blockage. The predicted peak overpressures ranged from 65.41 to 355.04 mbar, depending on obstacle orientation and position, compared with 100.53 mbar for the reference configuration. The reference LES configuration was assessed against experimental evidence, whereas the alternative layouts were evaluated numerically. These findings provide independent numerical evidence that equivalent global blockage does not necessarily imply equivalent explosion response. Experimental investigations on combustible dusts have also demonstrated that obstacle number, configuration and blockage ratio can significantly modify flame propagation, including non-monotonic responses under certain conditions (Yang et al., 2020; Zhang et al., 2024).

Taken together, these studies provide complementary evidence that geometrical congestion and its spatial organization can affect flame propagation and explosion overpressure, and that PDR-based numerical frameworks can reproduce selected experimentally observed congestion effects. The evidence nevertheless has different levels of applicability to the present investigation.

In most published FLACS benchmarks, numerical porosity and associated sub-grid contributions are derived from specified obstacle geometries. In contrast, the present rack and pallet configurations are represented by idealized regions with prescribed uniform area and volume porosities, without explicitly resolving the individual structural components. Equal nominal porosity therefore does not necessarily establish equivalence in obstacle surface area, local flow resistance, wake generation or flame–obstacle interaction. These distinctions are particularly relevant when transferring gas-explosion validation evidence to dust-explosion simulations.

Accordingly, the published FLACS/PDR benchmarks provide experimental support for the general numerical framework under the specific obstructed gas-explosion conditions investigated, while DESC/FLACS-DustEx studies offer complementary evidence for dust-explosion modelling. These findings provide a methodological basis for the present application, which employs idealized regions with prescribed uniform porosity within the established FLACS framework. However, the available benchmarks do not directly validate the physical equivalence between these porous regions and actual rack or pallet assemblies, nor the predicted magnitude or ranking of the rack–pallet pressure differences. The internal consistency of the calculated numerical response is examined separately in Section 4.4.

3.5. Unobstructed reference-case response

Following the final assessment, the spatial and temporal evolution of the unobstructed configuration was examined to establish the reference response for the subsequent assessment of obstacle effects. At the wall-adjacent monitoring location adopted for assessment, the static overpressure increased rapidly from approximately 0.115 bar(g) at $t = 0.120$ s to 0.339 bar(g) at $t = 0.140$ s. The maximum value of 0.341 bar(g) was reached at approximately $t = 0.141$ s. At $t = 0.154$ s, the pressure remained relatively high, approximately 0.316 bar(g), indicating that vent discharge and pressure redistribution continued after the occurrence of the principal peak.

Fig. 5 shows the evolution of static overpressure, temperature and combustion-product mass fraction in the vertical plane passing through the chamber center and vent opening. During the initial stage, the pressure disturbance propagated throughout a substantial portion of the enclosure, while the high-temperature and combustion-product regions remained concentrated around the central ignition location. The pressure wave therefore advanced ahead of the reacting region.

Before interacting with the vent, the thermal and combustion-product fields exhibited an approximately ellipsoidal expansion around the ignition source. In the absence of internal obstacles, no appreciable subdivision or deviation of the propagating front was observed. The expansion remained comparatively regular until the reacting region approached the vent opening.

At approximately $t = 0.140$ s, corresponding closely to the maximum monitored overpressure, an elevated pressure field occupied most of the chamber, with a pressure gradient developing towards the permanent vent. At the same instant, the high-temperature region and combustion products reached the opening and began to discharge into the external domain.

During the subsequent stage, represented at $t = 0.154$ s, the reacting products extended beyond the enclosure and formed a curved external jet. The interaction between the discharged flow, the vent boundaries and the surrounding fluid produced a non-uniform external structure with local recirculation. Meanwhile, the chamber remained positively pressurized, although the principal pressure maximum had already occurred.

The unobstructed configuration therefore provides a baseline characterized by relatively regular flame expansion, direct propagation towards the vent and the absence of obstacle-induced channelization, shielding or front fragmentation. The pressure and combustion patterns obtained for the rack and pallet configurations are compared against this reference in the following section.

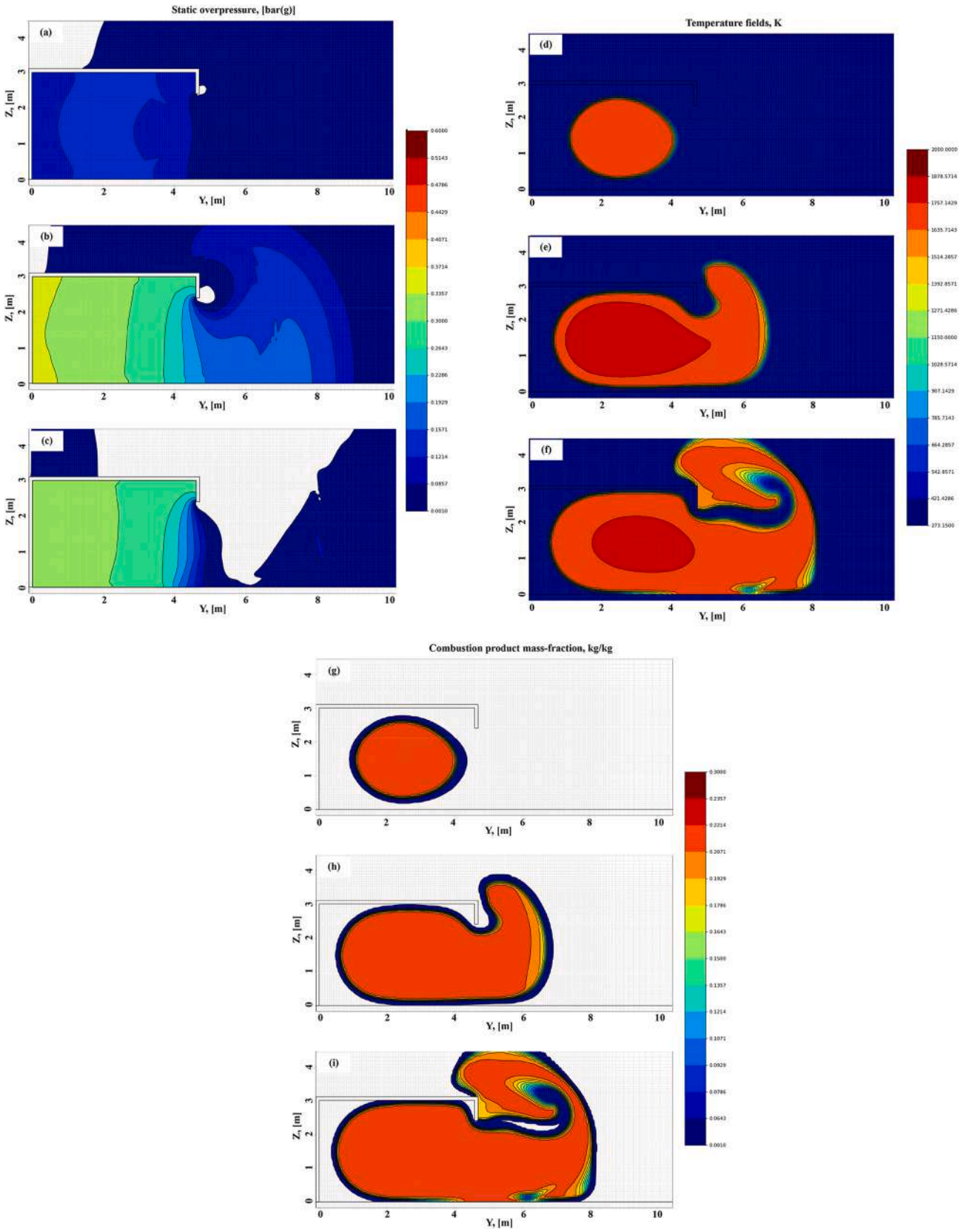

Fig. 5. Temporal evolution of the unobstructed reference configuration on the vertical plane at $x = 2.48$ m, at $t = 0.120$, 0.140 and 0.154 s: (a–c) static overpressure fields, (d–f) temperature fields and (g–i) combustion-product mass-fraction fields. The intermediate instant corresponds approximately to the maximum monitored overpressure.

4. Parametric investigation

Following the assessment of the numerical framework, a parametric investigation was conducted to evaluate the combined influence of obstacle porosity and spatial arrangement on vented dust explosion behavior. The calibrated geometry, computational domain, mesh, nominal dust concentration, ignition conditions, initial turbulence level and numerical control parameters were unchanged throughout the analysis. The geometrical envelope assigned to the initial dust cloud also remained unchanged. However, because the obstacle regions occupied a fraction of this envelope through the FLACS volume-porosity formulation, the effective fluid-accessible mixture volume, and consequently the total initial dust mass at the prescribed concentration, varied with obstacle porosity. Internal obstacles were then introduced according to two alternative storage layouts: two continuous rack-like regions and twelve discrete pallet-like regions.

The two configurations were specifically designed to have the same gross occupied volume. At each corresponding porosity, this controlled setup allowed the sensitivity of the numerical response to the prescribed spatial distribution and continuity of the obstacle regions to be examined without changing the gross obstacle volume. For each layout, the outer obstacle geometry was maintained unchanged across the investigated porosity cases. Area porosity and volume porosity were assigned the same prescribed value for each case using the standard FLACS-CFD DustEx geometry inputs. The equality between area and volume porosity was adopted as a controlled parametric modelling assumption, rather than as a geometrically derived representation of the flow openings and solid fraction of a specific physical storage system. This choice allowed the numerical influence of prescribed porosity and obstacle-region arrangement to be investigated consistently across the simulation matrix.

The adopted porosity parameter, ϕ, represents the open fraction of the obstacle region. Accordingly, $\phi = 0$ corresponds to a fully impermeable obstacle, whereas increasing values represent progressively more permeable regions. The values investigated were $\phi = 0, 0.4, 0.5, 0.6, 0.7, 0.8, 0.9$. The value $\phi = 1$ was not simulated because it would correspond to a completely open region and therefore to the unobstructed reference enclosure.

For the present configurations, the effective mixture volume can be expressed as $V_{mix} = V_{ch} - (1 - \phi)V_{obs}$, where $V_{ch} = 63.7\ m^3$ is the nominal chamber volume and $V_{obs} = 20.64\ m^3$ is the common gross obstacle volume. At the prescribed dust concentration of $0.250\ kg\ m^{-3}$, the corresponding initial dust mass therefore increased from 10.77 kg at $\phi = 0$ to 15.41 kg at $\phi = 0.9$, compared with 15.93 kg for the unobstructed enclosure. Importantly, because the rack and pallet layouts were assigned the same gross obstacle volume and the same porosity at each corresponding condition, their effective mixture volumes and initial dust masses were identical at equal ϕ.

Including the empty configuration, a total of fifteen simulations were analyzed: 1 *empty case* + 7 *rack cases* + 7 *pallet cases* = 15 *simulations*.

In the present investigation, the rack and pallet configurations were represented as idealized macroscopic volumes, with equal area and volume porosities prescribed directly through the standard FLACS-CFD DustEx modelling inputs rather than derived from individually resolved structural components. Consequently, the internal details of rack members, pallet loads and local openings are not geometrically resolved. The limiting condition $\varphi = 0$ corresponds to fully impermeable obstacle regions, whereas intermediate porosity values represent partially open regions within the adopted FLACS-CFD framework. This distinction is important because nominally equivalent porosity values do not necessarily imply identical physical flow resistance, turbulence generation or flame–obstacle interaction in real storage systems. The present parameterization is therefore intended to investigate the numerical sensitivity to obstacle-region permeability and spatial distribution under controlled modelling assumptions.

In addition to the wall-adjacent monitoring point adopted during model assessment, two further pressure-monitoring locations were introduced to provide a broader assessment of the internal pressure distribution. MP1 corresponded to the calibrated monitoring location on the lateral wall, MP2 was positioned at the center of the wall opposite the vent opening, and MP3 was located at the center of the enclosure roof. These three monitoring points were maintained unchanged in all simulations. The principal output quantities considered were the static-overpressure histories recorded inside the chamber, the maximum monitored overpressure, the maximum positive pressure-rise rate, $(dP/dt)_{max}$, the time of peak pressure, and the spatial evolution of temperature and combustion products. The pressure-rise rate was evaluated independently at MP1, MP2 and MP3 from the directly simulated pressure-time histories, and the highest positive value among the three monitoring locations was retained for each configuration. Extrapolated portions of incomplete pressure histories were not considered in the evaluation of $(dP/dt)_{max}$. The same monitoring locations and post-processing procedure were applied to all simulations.

4.1. Rack configuration and pressure response

The rack configuration consisted of two continuous rectangular regions positioned longitudinally inside the enclosure and separated by a central aisle. Each rack measured $1.0 \times 4.3 \times 2.4$ m, corresponding to a gross volume of $10.32\ m^3$. The total gross occupied volume of the two racks was therefore $V_{rack} = 20.64\ m^3$.

The rack geometry remained fixed throughout the investigation, while its assigned porosity was varied from 0 to 0.9. The continuous nature of the two obstacle regions created a longitudinal central passage extending towards the vent opening.

The adopted rack dimensions were selected with reference (European Committee for Standardization, 2022; European Committee for Standardization, 2021; European Committee for Standardization, 2008; Rack Manufacturers Institute, 2023), which provide the principal requirements for the structural design, specification, tolerances, clearances, testing and utilization of industrial pallet-racking systems. Accordingly, the $1.0 \times 4.3 \times 2.4$ m rack envelope was defined as a representative industrial-scale configuration rather than as a reproduction of a specific commercial product.

The two racks were centered along the longitudinal direction of the enclosure. Since their length was 4.3 m, compared with the internal chamber length of 4.6 m, a clearance of 0.15 m was maintained between each rack end and the corresponding chamber wall. The rack geometry and position remained unchanged throughout the parametric investigation. Only the porosity assigned to the two obstacle regions was varied. The geometry and arrangement of the rack configuration are shown in Fig. 6.

Fig. 7 presents the pressure-time histories obtained for the rack configuration at the three monitoring points considered in the analysis.

- MP1, located adjacent to the lateral wall at $(x, y, z) = (4.55, 1.20, 1.50)$ m;
- MP2, located at the centre of the wall opposite the vent at $(x, y, z) = (2.30, 0.05, 1.50)$ m;
- MP3, located below the centre of the enclosure roof at $(x, y, z) = (2.30, 2.30, 2.95)$ m.

All monitoring points were positioned in the fluid region, 0.05 m from the corresponding solid boundary. All porosity levels are included in the comparison together with the empty enclosure reference, allowing the effect of obstacle permeability on the internal pressure response to be evaluated at different positions inside the chamber.

At all monitoring points, the pressure histories exhibited a similar initial trend during the early stage of the event, indicating that the first compression phase was only weakly influenced by obstacle porosity.

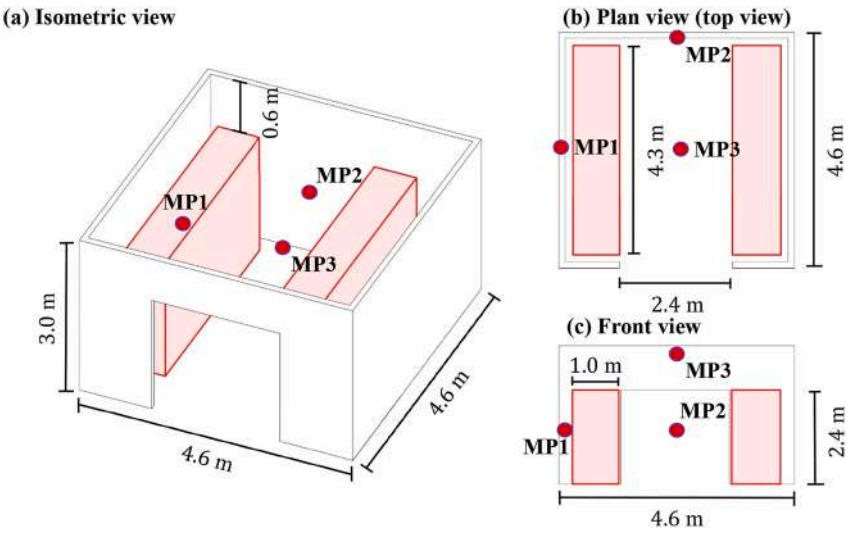

Fig. 6. Geometry of the continuous rack configuration: (a) isometric view, (b) plan view and (c) front view. The two longitudinal obstacle regions, each measuring $1.0 \times 4.3 \times 2.4$ m, are separated by a 2.4 m-wide central aisle aligned with the permanent vent opening. The enclosure dimensions are $4.6 \times 4.6 \times 3.0$ m.

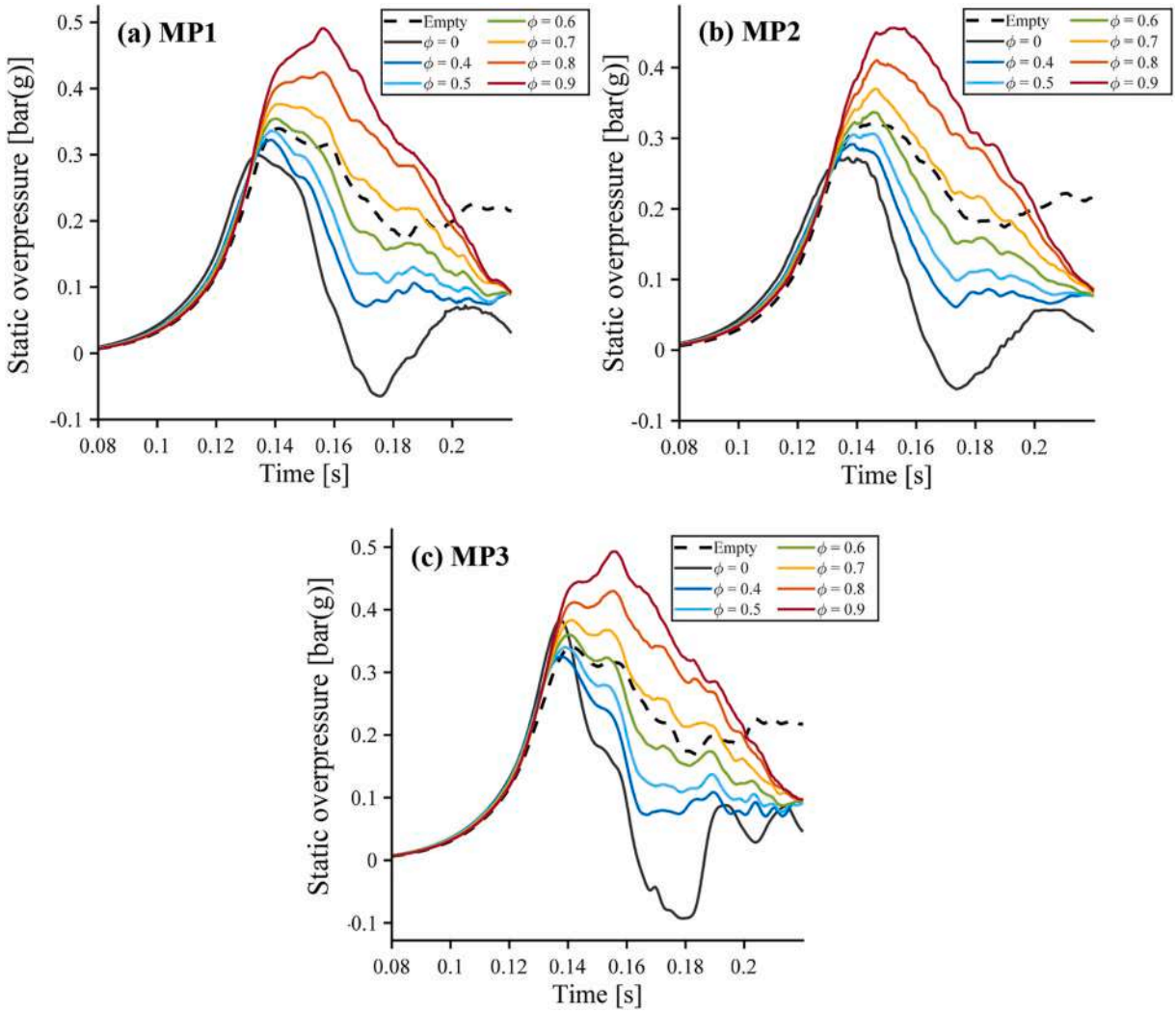

Fig. 7. Pressure-time histories for the rack configuration at (a) MP1, located on the lateral wall, (b) MP2, located at the center of the wall opposite the vent, and (c) MP3, located at the center of the roof, for the empty enclosure and all investigated porosity levels.

Differences became more evident near the peak and during the subsequent decay stage, where the influence of the rack permeability became significant. In general, the pressure response was strongly affected by porosity, both in terms of maximum overpressure and in terms of post-peak evolution.

A common feature observed in all three subfigures was that the case with $\phi = 0.4$ provided the lowest positive pressure response among the porous configurations, whereas increasing porosity beyond this value led to progressively higher peak pressures and a more sustained decay branch. In particular, the $\phi = 0.7$, $\phi = 0.8$, and $\phi = 0.9$ cases consistently produced the highest-pressure levels and maintained elevated pressure values for a longer time after the peak. This indicated that increasing permeability did not simply reduce confinement effects; rather, once a sufficiently open internal structure is reached, it favored a stronger interaction between flame propagation, gas expansion, and venting dynamics, resulting in a more severe pressure response.

The $\phi = 0$ case showed a distinct behavior with respect to the other configurations. Although its peak pressure was not always the lowest, the post-peak branch dropped much more rapidly and was followed by a marked pressure decay, with negative excursions visible in the signals, especially at MP3 and, to a lesser extent, at the other monitoring points. Within the adopted distributed-porosity framework, this behavior was consistent with a stronger separation between the prescribed obstructed and unobstructed regions and with a more rapid vent-driven pressure relief after the initial pressure build-up.

Among the three monitoring locations, MP3 generally recorded the highest peak pressure values, confirming that the roof region was the most critical location in terms of pressure loading. MP1 and MP2 showed the same overall porosity-dependent trend, although with slightly different amplitudes and local oscillations, reflecting the effect of wave propagation, reflection, and flow redistribution inside the enclosure.

Fig. 8 reports representative pressure contour plots for the rack configuration. In particular, the cases $\phi = 0$ and $\phi = 0.4$ are shown, since they are especially useful for highlighting how changes in permeability modify the pressure field inside the chamber and in the vented external region. The calculated contours were consistent with a pressure distribution influenced by the vent opening and the central free region between the two rack-like obstacles. They also indicated that the largest calculated pressure build-up occurred in the upper part of the enclosure and near the vent, consistently with the higher-pressure levels recorded at MP3.

Overall, within the adopted distributed-porosity framework, the results showed that the calculated pressure response of the rack configuration was not determined solely by the total obstructed volume. Variations in the prescribed rack permeability were associated with marked changes in both the magnitude and the temporal evolution of the calculated internal overpressure. In the present set of simulations, the $\phi = 0.4$ case corresponded to the minimum pressure response, whereas the highest and most persistent overpressures were observed for the most permeable configurations.

4.2. Pallet configuration and pressure response

The pallet configuration was developed to represent a storage arrangement in which the obstructed volume was distributed among several palletized load regions rather than concentrated within two continuous rack-like volumes. Twelve identical rectangular regions were arranged in four columns and three longitudinal rows, symmetrically positioned on the two sides of a central passage aligned with the permanent vent opening. The plan dimensions of each palletized region were 1.2×0.8 m, corresponding to the widely adopted 1200×800 mm pallet format (European Committee for Standardization, 2003) and included among the principal unit-load and pallet dimensions (International Organization for Standardization, 2003; International Organization for Standardization, 2012). These standards address pallet dimensions and their compatibility with pallet trucks, fork-lift trucks and other material-handling equipment. Other standard also requires the specification of storage layouts to consider the unit loads, the handling equipment and the intended configuration of the storage system (European Committee for Standardization, 2008). Accordingly, the adopted footprint was intended to provide a representative industrial palletized-load envelope rather than to reproduce a specific commercial

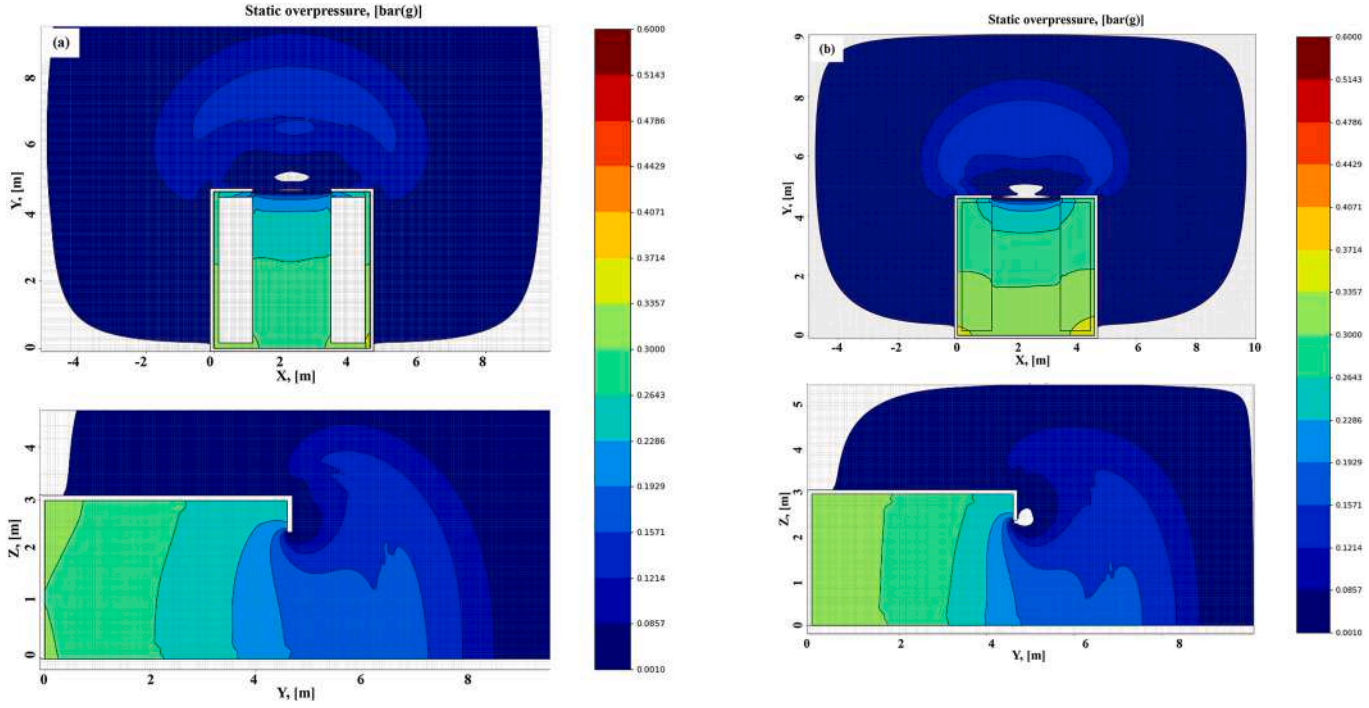

Fig. 8. Representative static overpressure contours for the rack configuration near the corresponding maximum-pressure stages: (a) impermeable rack regions, $\phi = 0$, at $t = 0.137$ s; and (b) porous rack regions, $\phi = 0.4$, at $t = 0.138$ s. For each case, the pressure field is shown on the horizontal XY plane at $z = 1.77$ m and on the vertical YZ plane at $x = 1.88$ m, illustrating the pressure distribution inside the enclosure and in the vented external region.

product. A 0.8 m-wide longitudinal passage was maintained between the two central pallet groups. This passage provided continuous access through the enclosure, preserved a material-handling corridor between the palletized regions and remained aligned with the vent opening. Its width should be interpreted as part of the geometrical idealization adopted within the available chamber dimensions rather than as a universal operational aisle width for a specific industrial truck, since the space required for truck manoeuvring depends on the characteristics of the selected handling equipment.

The height of the palletized regions was not taken from a prescribed commercial load dimension. Instead, it was calculated to obtain exactly the same gross occupied volume adopted for the rack configuration. The required height was therefore determined as 1.7917 m. Consequently, each palletized region occupied a gross volume of 1.72 m^3, and the total gross volume of the twelve regions was $V_{pallet} = 20.64\ m^3$.

The rack and pallet configurations therefore had identical gross occupied volumes. This volume equivalence was the principal constraint governing the selected pallet height and allowed the effect of obstacle spatial distribution to be separated from that of the total obstacle volume. The geometry and position of the twelve palletized regions remained unchanged in all simulations, while their assigned area and volume porosities were varied from $\phi = 0$ to $\phi = 0.9$. The geometry and arrangement of the pallet configuration are shown in Fig. 9.

Fig. 10 presents the pressure–time histories calculated at MP1, MP2 and MP3 for the pallet configuration. The unobstructed reference and all investigated porosity levels are included. As observed for the rack configuration, the signals recorded at the three monitoring points showed similar initial pressure-rise branches.

This spatial similarity indicated that the first compression wave propagated rapidly throughout the enclosure relative to the characteristic duration of the pressure rise. Differences among the monitoring points became more evident around the maximum pressure and during the post-peak phase, owing to local wave reflections, vent discharge and flow redistribution around the palletized regions.

The impermeable pallet configuration, $\phi = 0$, produced a markedly different response from the porous cases. Its maximum monitored overpressure was 0.252 bar(g), which was approximately 26.1% lower than the 0.341 bar(g) obtained for the empty enclosure.

In the adopted numerical representation, the solid palletized regions reduced the fluid-accessible combustible volume and modified the available propagation paths through the occupied regions. The resulting pressure response was consistent with shielding and flow-diversion effects associated with the prescribed solid regions; however, these mechanisms should be regarded as model-based interpretations of the calculated trend. An important increase occurred when the palletized regions were assigned a finite permeability. The maximum monitored pressure increased to 0.451 bar(g) at $\phi = 0.4$, already exceeding the empty-enclosure value by approximately 32.1%. It then increased progressively to 0.464, 0.485, 0.511, 0.542 and 0.586 bar(g) for $\phi = 0.5$, 0.6, 0.7, 0.8 and 0.9, respectively. Therefore, within the porous range $0.4 \leq \phi \leq 0.9$, the peak pressure followed a monotonic increasing trend.

The porous configurations also exhibited broader principal peaks and more sustained post-peak pressure branches than the impermeable case. Within the adopted distributed-porosity representation, increasing prescribed permeability allowed the numerical flow to penetrate a larger fraction of the nominally occupied regions. At the same time, the twelve discrete palletized regions retained multiple internal interfaces and passages in the numerical representation. These changes were associated with the progressively higher calculated pressure response obtained as the prescribed open fraction increased.

The three monitoring points reproduced the same overall porosity-dependent ordering. MP3 provided the maximum monitored value for the impermeable and low-to-intermediate porosity cases, whereas the global monitored maximum shifted to MP1 for $\phi = 0.8$ and $\phi = 0.9$. Nevertheless, the relatively small differences among the three pressure histories indicated that the principal enclosure pressurization remained predominantly global. The local position influenced the detailed peak amplitude and secondary oscillations but did not alter the main trend with porosity.

Fig. 11 compares representative pressure fields for the impermeable configuration, $\phi = 0$, and the high-pressure porous configuration, $\phi = 0.8$. The two cases were selected to illustrate the substantial differences in the calculated spatial pressure distribution associated with the prescribed obstacle permeability.

In the impermeable case, the calculated pressure field was comparatively less intense and exhibited patterns consistent with shielding and redirection associated with the prescribed solid palletized regions. The calculated field showed pressure relief through the central passage and the vent, together with lower-pressure regions downstream of the prescribed solid obstacles.

For $\phi = 0.8$, elevated pressures occupy a substantially larger portion of the chamber. The pressure field extends through the nominal palletized volumes, and a stronger pressure build-up is visible both within the enclosure and close to the vent-facing region. The external pressure

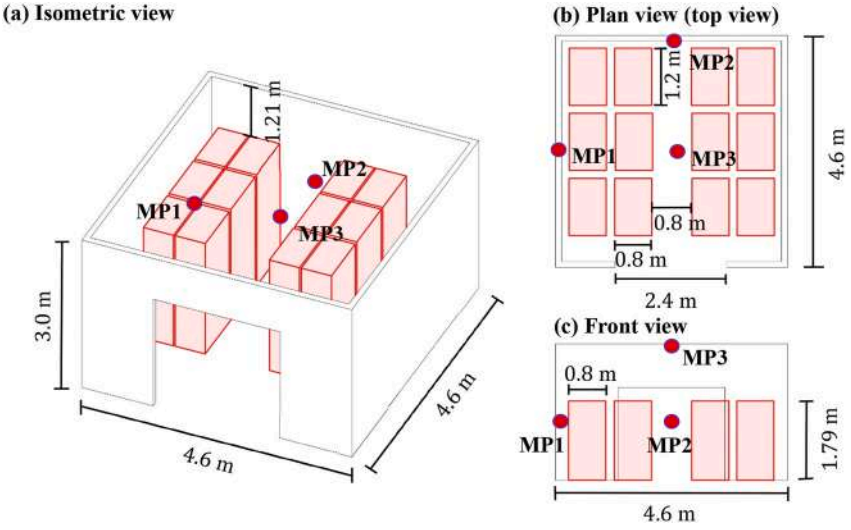

Fig. 9. Geometry of the discrete pallet configuration: (a) isometric view, (b) plan view and (c) front view. The twelve palletized regions, each measuring 0.8 × 1.2 × 1.79 m, are arranged symmetrically on the two sides of the 0.8 m-wide central passage aligned with the permanent vent opening. Adjacent palletized regions are separated by a distance of 0.15 m.

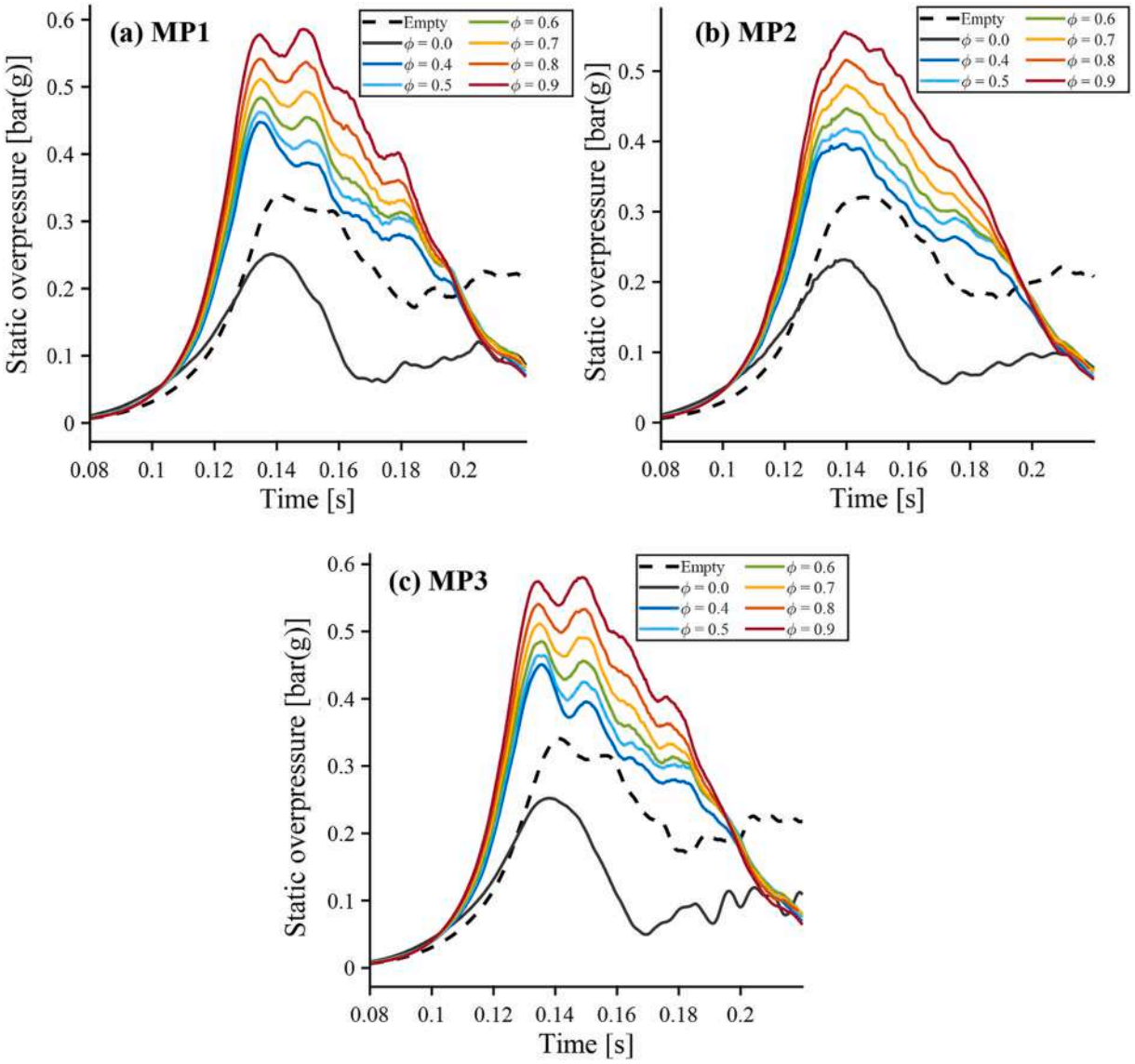

Fig. 10. Pressure–time histories for the pallet configuration at (a) MP1, located on the lateral wall, (b) MP2, located at the center of the wall opposite the vent, and (c) MP3, located at the center of the roof, for the empty enclosure and all investigated porosity levels.

disturbance is also more developed. These contours were consistent with the higher and more persistent pressure histories recorded at the monitoring points and indicated that, within the adopted numerical representation, changes in prescribed pallet permeability were associated with differences in both the peak magnitude and the spatial extent of the pressurized region.

Overall, within the investigated numerical framework, the pallet results showed that introducing the prescribed obstacle regions did not invariably increase the calculated explosion severity. The fully impermeable pallet representation produced a lower calculated pressure response than the empty enclosure, whereas the porous pallet representations were associated with substantial pressure amplification. Because increasing porosity also increased the effective fluid-accessible dust-cloud volume and the corresponding initial dust mass, the pressure increase across the porosity series could not be attributed exclusively to obstacle permeability and flow redistribution. Rather, the calculated response reflected the combined influence of the increasing combustible volume and fuel mass, together with the changing interaction among obstacle permeability, flow redistribution, pressure-wave propagation and vent discharge.

4.3. Direct comparison between rack and pallet layouts

Fig. 12 directly compares the maximum monitored static overpressure obtained for the rack and pallet configurations as a function of obstacle porosity. For each simulation, the reported value corresponds to the highest pressure recorded among MP1, MP2 and MP3. The horizontal dashed line represents the maximum monitored pressure of the unobstructed enclosure, equal to 0.341 bar(g).

The comparison confirmed that obstacle porosity alone was insufficient to describe the explosion response. Despite having the same gross occupied volume, the two layouts produced markedly different pressure levels, particularly under fully impermeable conditions. At $\phi = 0$, the rack configuration generated a maximum monitored overpressure of 0.383 bar(g), approximately 12.3% higher than the unobstructed reference. By contrast, the solid pallet configuration produced only 0.252 bar(g), corresponding to a reduction of approximately 26.1% relative to the empty enclosure.

For the fully impermeable configurations ($\phi = 0$), the maximum monitored overpressure was 0.383 bar(g) for the continuous rack arrangement and 0.252 bar(g) for the discrete pallet arrangement, corresponding to a rack pressure approximately 52.0% higher than the

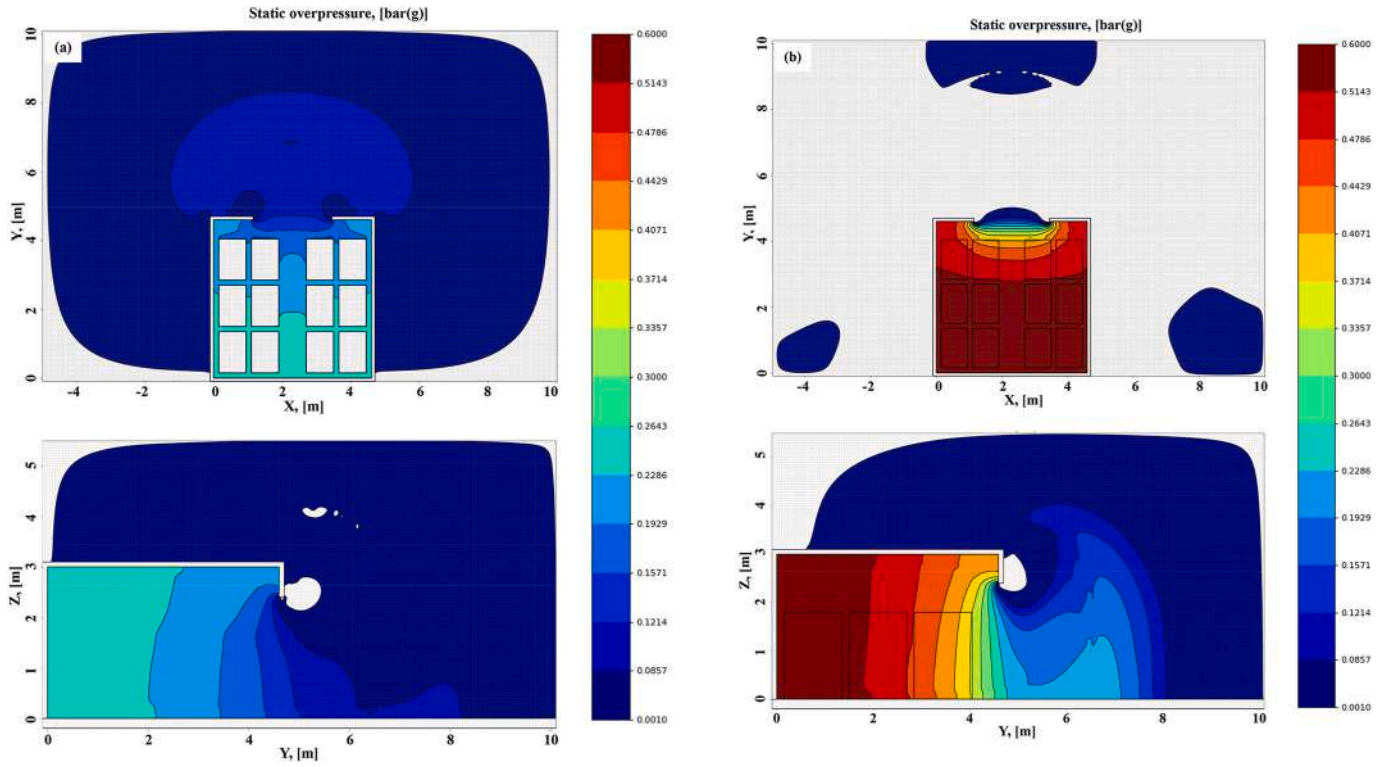

Fig. 11. Representative static overpressure contours for the pallet configuration near the corresponding maximum-pressure stages: (a) impermeable palletized regions, $\phi = 0$, shown on the horizontal XY plane at $z = 1.77$ m and $t = 0.136$ s, and on the vertical YZ plane at $x = 2.48$ m and $t = 0.139$ s; and (b) highly permeable palletized regions, $\phi = 0.8$, shown on the horizontal XY plane at $z = 1.77$ m and $t = 0.149$ s, and on the vertical YZ plane at $x = 1.88$ m and $t = 0.131$ s. The common contour scale highlights the substantially greater pressure build-up produced by the permeable configuration.

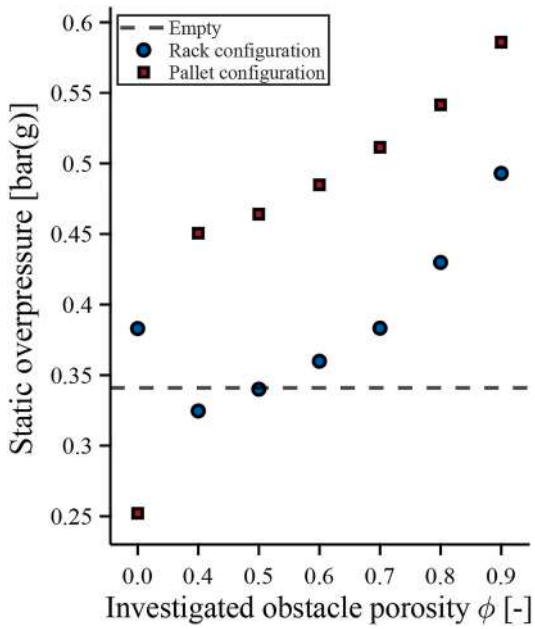

Fig. 12. Maximum monitored overpressure as a function of obstacle porosity for the continuous rack and discrete pallet configurations. The maximum value for each simulation was selected among the three monitoring points. The horizontal dashed line represents the maximum monitored overpressure obtained for the unobstructed enclosure.

pallet value. The continuous rack regions retained a longitudinal central passage aligned with the vent, whereas the twelve separate pallet regions introduced additional gaps and interfaces. These geometrical differences modified the spatial distribution of blocked volumes and available passages within the numerical model and were associated with different calculated pressure responses. However, because the structural details of actual storage systems were not resolved, these findings do not establish that the same quantitative pressure difference or underlying flow mechanisms would occur in physical rack and pallet configurations.

The rack configuration exhibited a non-monotonic response when the solid case was considered together with the porous cases. The maximum pressure decreased from 0.383 bar(g) at $\phi = 0$ to 0.325 bar(g) at $\phi = 0.4$. The latter value was approximately 4.8% below the unobstructed reference. At $\phi = 0.5$, the pressure was 0.340 bar(g), essentially coincident with the empty-enclosure value. For higher porosities, the pressure increased progressively, reaching 0.360, 0.383, 0.430 and 0.493 bar(g) at $\phi = 0.6$, 0.7, 0.8 and 0.9, respectively. The highest-porosity rack case therefore exceeded the unobstructed pressure by approximately 44.6%.

A different trend was obtained for the pallet configuration. The maximum pressure increased over the entire investigated porosity range, from 0.252 bar(g) at $\phi = 0$ to 0.451 bar(g) at $\phi = 0.4$. Further increases in porosity produced maximum pressures of 0.464, 0.485, 0.511, 0.542 and 0.586 bar(g) for $\phi = 0.5$, 0.6, 0.7, 0.8 and 0.9, respectively. All porous pallet configurations exceeded the unobstructed reference. The increase ranged from approximately 32.1% at $\phi = 0.4$ to 71.8% at $\phi = 0.9$. Within the porous range $0.4 \leq \phi \leq 0.9$, the pallet arrangement consistently produced higher pressures than the rack arrangement. At equal porosity, the pallet-to-rack pressure differences were approximately 38.8%, 36.5%, 34.8%, 33.5%, 26.0% and 18.9% for $\phi = 0.4$, 0.5, 0.6, 0.7, 0.8 and 0.9, respectively. Although the relative difference decreased with increasing porosity, the pallet configuration produced a higher maximum monitored overpressure than the rack configuration at every investigated porous condition within the adopted numerical framework.

Overall, the numerical results indicate that gross occupied volume and nominal porosity alone are insufficient to characterize the calculated response of the investigated obstacle layouts. Depending on the prescribed permeability and spatial arrangement, the maximum monitored overpressure could be lower than, comparable to, or higher than that obtained for the unobstructed enclosure. These findings highlight the importance of retaining the principal characteristics of obstacle continuity, orientation and spatial distribution in comparative numerical assessments of internally congested systems.

Within the adopted distributed-porosity modelling framework, continuous and discrete obstacle layouts characterized by identical gross occupied volume and nominal porosity produced different calculated explosion responses. These results highlight the importance of retaining the principal characteristics of obstacle spatial distribution, continuity and orientation in numerical representations of internally congested enclosures.

The quantitative results are summarized in Tables 5 and 6. Table 5 reports the maximum monitored overpressures and the corresponding variations relative to the unobstructed enclosure, whereas Table 6 identifies the critical monitoring location and the direct pressure difference between the pallet and rack configurations.

Within the adopted distributed-porosity framework, the different numerical responses of the rack and pallet configurations may be associated with the different spatial distribution of the prescribed obstacle regions and with the resulting interaction between the expanding flow, internal passages and vent discharge. However, the present simulations do not resolve the detailed local geometry of real rack or pallet systems, and no case-specific experimental or independently validated geometrically resolved numerical comparison was available for the investigated configurations. Accordingly, the calculated differences between rack and pallet layouts should be interpreted as model-dependent comparative responses within the adopted FLACS-CFD distributed-porosity framework. Findings such as the opposite response of the impermeable rack and pallet cases and the higher pressures calculated for the porous pallet configurations cannot presently be generalized as physical rankings of real rack and pallet systems. Experimental testing of internally congested dust explosions or comparison with an independently validated geometrically resolved model would be required to establish whether these quantitative trends are reproduced outside the present modelling framework.

These results do not imply that increasing porosity will universally increase explosion pressure. The observed trends apply to the investigated enclosure, obstacle geometries, vent arrangement and porosity range, and should be interpreted within the adopted distributed-porosity modelling framework. More generally, the prescribed porosity controls the extent to which the numerical flow can penetrate an obstacle region, whereas the spatial arrangement determines where these interactions occur and how the available propagation paths are represented. Nominal porosity should therefore be interpreted as a geometry-dependent modelling parameter rather than as a complete or universally transferable descriptor of internal congestion.

To complement the comparison based on maximum overpressure, the maximum positive pressure-rise rate, $(dP/dt)_{max}$, was also evaluated for all configurations. The resulting values and corresponding critical monitoring locations are summarized in Table 7.

The pressure-rise-rate results provided complementary information to the maximum-overpressure comparison. The unobstructed reference configuration produced $(dP/dt)_{max} = 15.76$ bar s^{-1} at MP1, whereas all investigated rack and pallet configurations exhibited higher maximum positive pressure-rise rates. For the rack arrangement, $(dP/dt)_{max}$ ranged from 20.16 to 31.58 bar s^{-1}, with the highest value obtained for the impermeable configuration. The response was non-monotonic with porosity. For the pallet arrangement, the corresponding values ranged from 21.02 to 43.19 bar s^{-1}, with the highest value occurring at $\phi = 0.7$. Except for the impermeable case, the pallet configuration produced higher maximum pressure-rise rates than the corresponding rack configuration. The critical location also differed from that identified from the maximum-overpressure analysis: MP2 governed all pallet cases and all porous rack cases, whereas MP3 governed the impermeable rack configuration. These results indicated that obstacle arrangement affected not only the maximum pressure magnitude but also the transient rate at which the pressure loading developed.

The variation of effective mixture volume with porosity should also be considered when interpreting the trends across different ϕ values. Since the nominal dust concentration was maintained, increasing obstacle porosity increased both the fluid-accessible volume occupied by the mixture and the corresponding total dust mass. Consequently, the variation of pressure with porosity reflected the combined influence of obstacle permeability, available combustible volume and fuel mass. This coupling prevented the porosity-series results from being interpreted as a pure isolated effect of permeability. In contrast, the direct rack-to-pallet comparison at each fixed porosity was not affected by this issue, because the two layouts had identical gross obstacle volume, identical nominal porosity, identical effective mixture volume and, consequently, identical initial dust mass. The differences observed between rack and pallet configurations at equal ϕ could therefore be associated with their different spatial arrangement within the adopted distributed-porosity framework.

Table 5
Maximum monitored overpressures for the rack and pallet configurations and corresponding variations relative to the unobstructed enclosure. The maximum monitored overpressure for the empty reference configuration is0.341 bar(g).

ϕ	Rack P_{max} [bar (g)]	Rack vs empty [%]	Pallet P_{max} [bar (g)]	Pallet vs empty [%]
0.0	0.383	+12.3	0.252	−26.1
0.4	0.325	−4.8	0.451	+32.1
0.5	0.340	−0.3	0.464	+36.1
0.6	0.360	+5.5	0.485	+42.2
0.7	0.383	+12.4	0.511	+50.0
0.8	0.430	+26.1	0.542	+58.8
0.9	0.493	+44.6	0.586	+71.8

Table 6
Direct comparison between the rack and pallet configurations in terms of critical monitoring location and percentage difference in maximum overpressure. Positive values indicate higher pressures for the pallet configuration.

ϕ	Rack critical MP	Pallet critical MP	Pallet vs rack [%]
0.0	MP3	MP3	−34.2
0.4	MP3	MP3	+38.8
0.5	MP3	MP3	+36.5
0.6	MP3	MP3	+34.8
0.7	MP3	MP3	+33.5
0.8	MP3	MP1	+26.0
0.9	MP3	MP1	+18.9

Table 7
Maximum positive pressure-rise rates and corresponding critical monitoring locations for the rack and pallet configurations. For each simulation, $(dP/dt)_{max}$ corresponds to the highest positive pressure derivative obtained among MP1, MP2 and MP3. Only directly simulated pressure histories were considered. The unobstructed reference configuration produced $(dP/dt)_{max} = 15.76$ bar s^{-1} at MP1.

ϕ	Rack $(dP/dt)_{max}$ [bar s^{-1}]	Rack critical MP	Pallet $(dP/dt)_{max}$ [bar s^{-1}]	Pallet critical MP
0.0	31.58	MP3	21.02	MP2
0.4	21.93	MP2	31.05	MP2
0.5	20.16	MP2	38.72	MP2
0.6	28.30	MP2	39.71	MP2
0.7	25.19	MP2	43.19	MP2
0.8	29.93	MP2	33.94	MP2
0.9	30.80	MP2	37.62	MP2

4.4. Internal consistency assessment of the rack–pallet numerical response

To complement the external benchmark assessment presented in Section 3.4, an additional internal consistency assessment was conducted using the results of the fifteen simulations already performed. The objective was to examine whether the differences between the rack and pallet configurations were consistently reflected in multiple pressure-related response indicators, rather than being restricted to the maximum monitored overpressure. The assessment considered two quantities: the maximum monitored static overpressure, $P_{red,max}$, and the maximum positive pressure-rise rate, $(dP/dt)_{max}$. Both quantities were evaluated using the three monitoring locations described in Section 4, without introducing additional numerical simulations or modifying the adopted modelling assumptions.

For each corresponding rack–pallet pair, the gross obstacle volume, prescribed porosity, effective fluid-accessible volume, initial dust mass, ignition conditions and numerical settings were identical. Consequently, the paired comparisons isolate the sensitivity of the calculated response to the spatial distribution of the prescribed obstacle regions under otherwise equivalent numerical conditions. The relative difference between the two configurations was evaluated as: $\Delta X = 100 \cdot (X_{pallet} - X_{rack})/X_{rack}$, where X represents either $P_{red,max}$ or $(dP/dt)_{max}$. Positive values indicate higher calculated responses for the pallet configuration.

The fully impermeable configurations ($\phi = 0$) provide a limiting-case comparison in which the prescribed obstacle regions behave as completely solid volumes, without intermediate permeability within their geometrical envelopes. Under these conditions, the rack configuration produced a maximum monitored overpressure of 0.383 bar(g), whereas the corresponding pallet configuration produced 0.252 bar(g). Compared with the unobstructed reference pressure of 0.341 bar(g), these values represent an increase of approximately 12.3% for the rack layout and a reduction of approximately 26.1% for the pallet layout. The corresponding maximum positive pressure-rise rates were 31.58 bar/s and 21.02 bar/s, respectively. Therefore, the impermeable pallet configuration exhibited reductions of approximately 34.2% in maximum overpressure and 33.4% in maximum positive pressure-rise rate relative to the impermeable rack configuration.

This limiting-case comparison indicates that the calculated sensitivity to spatial arrangement is not exclusively associated with the assignment of intermediate porosity values. Even when the obstacle regions are fully impermeable, the different distribution of continuous and discrete solid volumes produces different numerical pressure responses. Nevertheless, this finding does not constitute independent validation of the underlying geometrical effects, as both configurations remain represented within the same CFD framework and computational discretization.

For the partially porous configurations ($\phi = 0.4$–0.9), a different but consistent ordering was obtained. As discussed in Section 4.3, the pallet configuration produced higher maximum monitored overpressures than the rack configuration at every investigated porous condition. The relative increase ranged from approximately 18.9% to 38.8%. The comparison was therefore extended to the maximum positive pressure-rise rates to determine whether the same ordering was observed for an additional response indicator.

As shown in Table 8, the pallet configuration exhibited higher maximum positive pressure-rise rates than the rack configuration for all six partially porous conditions. The relative increases ranged from approximately 13.4% at $\phi = 0.8$ to 92.1% at $\phi = 0.5$. Although the magnitude of the difference varied considerably with porosity, its sign remained consistent with that obtained from the maximum-overpressure comparison. Conversely, for $\phi = 0$, both indicators showed lower values for the pallet configuration. Thus, the same rack–pallet ordering was obtained for both pressure-related quantities across all seven investigated porosity levels.

Table 8
Relative differences between the pallet and rack configurations in maximum monitored overpressure and maximum positive pressure-rise rate at equal prescribed porosity. Positive values indicate higher responses for the pallet configuration.

Prescribed porosity ϕ [–]	$\Delta P_{red,max}$ [%]	$\Delta(dP/dt)_{max}$ [%]
0.0	−34.2	−33.4
0.4	+38.8	+41.6
0.5	+36.5	+92.1
0.6	+34.8	+40.3
0.7	+33.5	+71.5
0.8	+26.0	+13.4
0.9	+18.9	+22.1

Note: Maximum-overpressure differences are taken from the direct comparisons reported in Section 4.3. Pressure-rise-rate differences are calculated from the rounded values reported in Table 7. Both quantities correspond to the maximum value recorded among the three monitoring points for each configuration.

The spatial locations associated with these extrema were also considered. For maximum monitored overpressure, MP3 was generally critical for the rack configuration, whereas the critical location for the pallet configuration shifted from MP3 to MP1 at $\phi = 0.8$ and $\phi = 0.9$. In contrast, the maximum positive pressure-rise rate occurred at MP2 for both configurations throughout the partially porous range. Therefore, the agreement in pressure-rise-rate ordering for the porous cases was obtained at the same monitoring location, although the corresponding maxima were not necessarily reached at identical times. This distinction is relevant because the global maximum overpressure and maximum pressure-rise rate characterize different aspects of the transient pressure response and may occur at different locations within the enclosure.

The observed agreement between the two indicators provides an additional internal consistency check of the numerical trends obtained for the rack and pallet configurations. In particular, the higher maximum overpressures predicted for the partially porous pallet configurations were accompanied by higher maximum positive pressure-rise rates, whereas the opposite ordering was observed under fully impermeable conditions. However, maximum overpressure and pressure-rise rate are derived from the same numerical solutions and are therefore not statistically or physically independent validation datasets. Their agreement cannot, by itself, exclude systematic errors associated with the distributed-porosity representation, unresolved obstacle geometry, sub-grid resistance modelling or numerical discretization.

Furthermore, the grid-sensitivity assessment presented in Section 3 was conducted for the unobstructed reference configuration and does not directly establish grid independence for the internally congested cases. The present analysis should therefore be understood as a verification of the internal coherence of the available numerical results, rather than as a direct validation of the quantitative pressure differences predicted for real rack and pallet systems.

Overall, the combined limiting-case and cross-metric comparisons show that the calculated influence of obstacle spatial arrangement is systematically reflected in both maximum monitored overpressure and maximum positive pressure-rise rate within the adopted modelling framework. Together with the independent experimental and numerical evidence discussed in Section 3.4, these findings strengthen the technical basis for investigating spatial arrangement as a relevant parameter in internally congested explosion scenarios, while retaining the distinction between internally consistent numerical predictions and experimentally validated physical behavior.

5. Implications for congestion modelling and vented-explosion assessment

The results of the present investigation provide further insight into the role of obstacle porosity and spatial arrangement in the numerical assessment of vented dust explosions. In particular, the comparison between continuous rack-like regions and discrete palletized regions indicates that identical gross obstacle volumes and prescribed porosity values do not necessarily lead to equivalent calculated pressure responses. However, the engineering significance of these findings must be evaluated in conjunction with the external benchmark evidence presented in Section 3.4 and the internal consistency assessment reported in Section 4.4.

The published experimental benchmarks provide an important basis for assessing the applicability of the FLACS distributed-porosity framework to internally congested environments. Previous investigations have demonstrated that FLACS can reproduce selected congestion-related pressure trends in vented gaseous deflagrations, including configurations with different obstruction levels and arrangements (Pedersen and Middha, 2012; Diakow et al., 2018; Lucas et al., 2021). Nevertheless, the quantitative comparisons discussed in Section 3.4 also reveal substantial discrepancies in absolute overpressure predictions under certain conditions. These findings indicate that the representation of obstacle-induced flow resistance, turbulence generation and flame acceleration remains sensitive to the adopted numerical formulation and geometrical description.

For combustible dusts, the experimental investigations conducted by Skjold et al. (2014), together with previous assessments of DESC and FLACS-DustEx (Skjold et al., 2006; Castellanos et al., 2013; Tascón and Aguado, 2017), provide complementary evidence concerning the modelling of dust-flame propagation, pressure development and venting phenomena. However, these studies do not establish the predictive accuracy of the specific homogeneous porous regions adopted in the present rack and pallet configurations. The available validation evidence therefore supports different components of the numerical methodology, rather than providing a direct experimental verification of the investigated layouts.

Independent investigations further support the physical relevance of obstacle spatial arrangement. Mahesh et al. (2025) demonstrated through geometrically resolved large-eddy simulations that changing obstacle orientation and position while maintaining constant volume and area blockage can produce substantial differences in explosion overpressure. Their results indicate that global blockage parameters alone do not uniquely determine the numerical response of a congested enclosure. Experimental studies involving combustible dusts have similarly demonstrated that obstacle number, blockage ratio and geometrical arrangement can affect flame propagation, sometimes producing non-monotonic responses (Yang et al., 2020; Zhang et al., 2024). Although these investigations differ from the present study in terms of fuel properties, geometry and numerical methodology, they provide independent support for treating obstacle spatial distribution as a relevant parameter in explosion analysis.

The comparison between these independent findings and the present results is particularly relevant. In the adopted FLACS-CFD DustEx framework, the two continuous rack regions and twelve discrete pallet regions were assigned identical gross occupied volumes and nominal porosities at each corresponding condition. Nevertheless, the resulting maximum monitored overpressures differed considerably. For the partially porous configurations, the pallet layout produced maximum overpressures approximately 18.9–38.8% higher than the corresponding rack layout. The additional assessment presented in Section 4.4 showed that this ordering was also reproduced by the maximum positive pressure-rise rates, whereas the fully impermeable configurations exhibited the opposite ordering for both indicators.

These observations suggest that the calculated response is systematically sensitive to the prescribed spatial organization of the obstacle regions and is not restricted to a single pressure-related quantity. The fully impermeable configurations provide an additional limiting-case comparison, since differences between continuous and discrete obstacle arrangements remain present without intermediate permeability inside the prescribed regions. However, the agreement between maximum overpressure and maximum pressure-rise rate represents an internal consistency check rather than independent validation, because both indicators originate from the same numerical solutions and modelling assumptions.

An important distinction concerns the interpretation of the porosity parameter itself. In conventional FLACS applications involving geometrically specified obstacles, area and volume porosities and associated sub-grid contributions can be derived from the underlying geometrical description. In contrast, the present study applied the established FLACS/PDR framework to idealized macroscopic rack and pallet regions, with equal area and volume porosities prescribed directly through the standard modelling inputs. This procedure follows an established numerical formulation but does not reconstruct the detailed geometry of individual structural members, pallet loads or local openings. Equivalent nominal porosity values therefore do not necessarily imply equivalent physical resistance, obstacle surface area, wake generation or flame–obstacle interaction.

This distinction represents a limitation in transferring the available experimental validation evidence to the present configurations. In particular, the benchmark studies do not demonstrate that uniformly prescribed porous regions reproduce the same local flow and combustion mechanisms as geometrically resolved storage systems. Although the independent evidence supports the physical significance of spatial arrangement, it does not establish that the quantitative differences predicted between the investigated rack and pallet layouts would be reproduced in corresponding physical experiments. Accordingly, the present findings should be interpreted as a comparative assessment of spatial-arrangement sensitivity within the adopted distributed-porosity framework.

The interpretation of the porosity-dependent pressure trends also requires consideration of the combustible mixture volume. In the present simulations, increasing the prescribed porosity increased the fluid-accessible volume and, at the fixed nominal dust concentration, the total initial dust mass. Consequently, the pressure variations observed across different porosity values reflect the combined effects of permeability, available combustible volume and initial fuel mass. These contributions cannot be separated completely using the current simulation matrix. In contrast, the paired comparison between rack and pallet configurations at each fixed porosity was performed with identical effective mixture volumes and initial dust masses, providing a more controlled assessment of the influence of the prescribed spatial arrangement.

The geometrical organization of the obstacle regions may also influence the spatial distribution of the calculated pressure loading. In the rack configurations, the maximum monitored overpressure was consistently recorded at the roof monitoring point MP3. For the pallet configurations, the critical location shifted from MP3 to the lateral-wall monitoring point MP1 at the two highest investigated porosities. Conversely, the maximum positive pressure-rise rate for the partially porous configurations was recorded at MP2 for both layouts. These differences indicate that the prescribed spatial arrangement can affect the location and temporal characteristics of the calculated pressure extrema, in addition to their magnitude.

From an engineering perspective, these findings highlight the importance of considering the spatial characteristics of internal congestion when constructing numerical representations of non-standard industrial enclosures. Aggregate descriptors such as occupied volume, average blockage ratio and nominal porosity remain useful for characterizing the overall degree of obstruction, but they do not fully describe the number, continuity, orientation and spacing of obstacle regions. When such geometrical information is available, retaining the principal features of the internal layout may provide a more informative

numerical representation than adopting a single equivalent obstruction parameter.

Nevertheless, the present results should not be used to derive universal correction factors for explosion vent sizing or to establish a general severity ranking between physical rack and pallet systems. The quantitative predictions remain specific to the investigated enclosure, permanent vent, centrally ignited maize-starch cloud, initial conditions, numerical resolution and prescribed obstacle representations. Furthermore, the grid-sensitivity assessment was performed for the unobstructed reference configuration and does not independently establish grid convergence for the congested cases. Additional experimental measurements or independently validated, geometrically resolved simulations would be required to establish the quantitative transferability of the predicted rack–pallet differences.

Overall, the combination of published experimental benchmarks, independent investigations of obstacle-arrangement effects and the internal consistency assessment provides a broader technical basis for interpreting the present numerical results. These complementary findings support the relevance of spatial arrangement as a parameter in the analysis of internally congested explosions and demonstrate that its influence is not exclusive to FLACS-based investigations. However, they do not fully exclude systematic effects associated with the specific distributed-porosity parameterization. The principal contribution of the present study is therefore the identification and quantitative characterization of spatial-arrangement sensitivity under controlled numerical conditions, supported by external evidence concerning the physical importance of congestion topology, rather than a direct validation of the pressure response of real rack and pallet systems.

6. Conclusions

This study investigated the combined influence of obstacle porosity and spatial arrangement on vented dust explosions using the FLACS-CFD DustEx numerical framework. An unobstructed reference enclosure was compared with two internally congested configurations consisting of two continuous rack-like regions and twelve discrete palletized regions. The two layouts were characterized by identical gross obstacle volumes and were investigated over a prescribed porosity range of $\phi = 0 - 0.9$. At each corresponding porosity, the effective fluid-accessible mixture volume, initial dust mass, ignition conditions and numerical settings were maintained identical, allowing the influence of the prescribed spatial arrangement to be examined under controlled numerical conditions.

The unobstructed reference configuration produced a maximum monitored overpressure of 0.341 bar(g). The introduction of internal obstacles resulted in different pressure responses depending on the assigned porosity and spatial arrangement. Under fully impermeable conditions ($\phi = 0$), the rack configuration produced a maximum overpressure of 0.383 bar(g), approximately 12.3% above the unobstructed reference, whereas the pallet configuration produced 0.252 bar(g), approximately 26.1% below the reference. These results demonstrated that the two prescribed solid-obstacle arrangements could produce opposite numerical effects on pressure development despite having the same gross occupied volume.

For the partially porous configurations ($\phi = 0.4 - 0.9$), maximum monitored overpressure increased from 0.325 to 0.493 bar(g) for the rack layout and from 0.451 to 0.586 bar(g) for the pallet layout. At equal porosity, the pallet configuration consistently produced maximum overpressures approximately 18.9–38.8% higher than those obtained for the rack configuration. However, increasing porosity also increased the effective combustible mixture volume and the total initial dust mass at the prescribed concentration. Therefore, the observed pressure variations across different porosity levels reflect the combined influence of obstacle permeability, available combustible volume and fuel mass, rather than an isolated permeability effect.

The additional internal consistency assessment showed that the rack–pallet ordering observed in maximum monitored overpressure was also reproduced by the maximum positive pressure-rise rate. For all partially porous conditions, the pallet configuration produced higher values of both response indicators, whereas the fully impermeable condition exhibited the opposite ordering. Moreover, the critical monitoring location for maximum overpressure varied with obstacle arrangement, indicating that the prescribed spatial distribution influenced both the magnitude and the location of the calculated pressure extrema. These findings demonstrate systematic consistency across the investigated pressure-related indicators, although they do not constitute independent validation because the quantities originate from the same numerical solutions.

To strengthen the assessment of the adopted methodology, published experimental benchmarks involving FLACS simulations of obstructed gaseous deflagrations were examined together with experimental investigations of dust explosions and independent numerical studies of obstacle-arrangement effects. The available evidence shows that PDR-based numerical approaches can reproduce selected experimentally observed congestion-related pressure trends, although substantial discrepancies in absolute overpressure predictions remain possible. Investigations using geometrically resolved large-eddy simulations and experimental dust-flame measurements further support the physical relevance of obstacle arrangement, independently of the specific FLACS-CFD framework.

Published experimental benchmarks support the general FLACS/PDR methodology for selected obstructed gas-explosion configurations, while DESC/FLACS-DustEx studies provide complementary evidence for dust-explosion modelling. The present rack and pallet simulations employed the established FLACS numerical framework, assigning equal area and volume porosities directly to idealized macroscopic regions rather than deriving them from explicitly resolved storage geometries. Therefore, the general numerical methodology is supported by experimental evidence in the literature, whereas its application to these simplified rack and pallet configurations is methodologically supported but has not been directly validated against equivalent physical systems. Consequently, the quantitative transferability of the predicted rack–pallet pressure differences remains unverified. The principal conclusion is therefore that identical gross obstacle volume and nominal porosity do not necessarily produce equivalent calculated vented-explosion responses when applied to different spatial arrangements within the adopted distributed-porosity framework. The external benchmark assessment and internal consistency analysis strengthen the technical interpretation of this result and support the physical relevance of investigating obstacle topology. However, they do not fully exclude systematic effects associated with the prescribed porosity representation, unresolved obstacle geometry or numerical discretization.

The present conclusions remain specific to the investigated enclosure, permanent vent, centrally ignited maize-starch cloud and selected obstacle representations. The combustion parameterization and grid-sensitivity assessment were established using the unobstructed reference configuration, and their predictive accuracy and grid convergence were not independently verified for the internally congested cases. Accordingly, the calculated rack–pallet pressure differences should not be interpreted as experimentally validated physical rankings or as universal correction factors for explosion vent sizing.

Future investigations should prioritize experimental benchmarks involving internally congested dust-explosion enclosures and comparisons between prescribed distributed-porosity regions and geometrically resolved obstacle representations. Attention should be given to the effects of local flow resistance, turbulence generation, flame–obstacle interaction and grid resolution. Such investigations would provide the additional evidence required to establish the quantitative transferability of the present findings to real industrial storage configurations.

CRediT authorship contribution statement

F. Pinna: Writing – review & editing, Writing – original draft, Visualization, Validation, Software, Methodology, Investigation, Formal analysis. **M. Zucca:** Writing – review & editing, Project administration. **M. Simoncelli:** Writing – review & editing, Project administration, Funding acquisition. **F. Stochino:** Writing – review & editing, Validation, Supervision, Resources, Project administration, Methodology, Funding acquisition, Conceptualization.

Declaration of competing interest

The authors declare that they have no known competing financial interests or personal relationships that could have appeared to influence the work reported in this paper.

Data availability

Data will be made available on request.

References

Abbasi, T., Abbasi, S.A., 2007. Dust explosions–Cases, causes, consequences, and control. J. Hazard Mater. 140 (1–2), 7–44. https://doi.org/10.1016/j.jhazmat.2006.11.007.

Alauddin, M., Addo, A., Pegg, M.J., Amyotte, P., 2026. Using dimensional analysis to assess dust explosion severity. J. Loss Prev. Process. Ind., 105797 https://doi.org/10.1016/j.jlp.2025.105797.

Castellanos, D., Skjold, T., van Wingerden, K., Eckhoff, R.K., Mannan, M.S., 2013. Validation of the DESC code in simulating the effect of vent ducts on dust explosions. Ind. Eng. Chem. Res. 52, 6057–6067. https://doi.org/10.1021/ie4004943.

Dhiman, M., Zambare, A., Sathiah, P., Narasimhamurthy, V.D., 2023. CFD simulations of vapour cloud explosions using PDRFoam. J. Loss Prev. Process. Ind. 85, 105164. https://doi.org/10.1016/j.jlp.2023.105164.

Diakow, P.A., Thomas, J.K., Vivanco, E., 2018. Comparison of large-scale vented deflagration tests to CFD simulations for partially congested enclosures. J. Loss Prev. Process. Ind. 56, 147–154. https://doi.org/10.1016/j.jlp.2018.07.012.

European Committee for Standardization, 2003. Pallet Production specification—Part 1: Construction Specification for 800 mm × 1200 mm Flat Wooden Pallets (EN 13698-1:2003). CEN. Retrieved from. https://knowledge.bsigroup.com/products/pallet-production-specification-construction-specification-for-800-mm-x-1200-mm-flat-wooden-pallets.

European Committee for Standardization, 2008. EN 15629:2008: steel static storage systems—Specification of storage equipment. Retrieved from. https://shop.standards.ie/en-ie/standards/en-15629-2008-326876_saig_cen_cen_753064/.

European Committee for Standardization, 2021. EN 15620:2021: steel static storage systems—Tolerances, deformations and clearances. Retrieved from. https://shop.standards.ie/en-ie/standards/en-15620-2021-326866_saig_cen_cen_3016225/.

European Committee for Standardization, 2022. EN 15512:2020+A1:2022: steel static storage systems—Adjustable pallet racking systems—Principles for structural design. Retrieved from. https://shop.standards.ie/en-ie/standards/en-15512-2020-a1-2022-326727_saig_cen_cen_3125293/.

European Committee for Standardization (CEN), 2012. EN 14491: Dust Explosion Venting Protective Systems. CEN. Retrieved from. https://store.uni.com/uni-en-14491-20.

Gexcon, A.S., 2025. FLACS-CFD 24.2 user's manual. Gexcon AS. https://knowledge.gexcon.com/.

Hansen, O.R., Renoult, J., Sherman, M.P., Tieszen, S.R., 2005. Validation of FLACS-hydrogen CFD consequence prediction model against large scale H_2 explosion experiments in the FLAME facility. Proceedings of the International Conference on Hydrogen Safety, Pisa, Italy. https://conference.ing.unipi.it/ichs2005/ichs.pdf.

Huang, C., Bloching, M., Lipatnikov, A.N., 2022. A vented corn starch dust explosion in an 11.5 m3 vessel: experimental and numerical study. J. Loss Prev. Process. Ind. 75, 104707. https://doi.org/10.1016/j.jlp.2021.104707.

Huang, C., Lipatnikov, A.N., Lövström, C., Smajovic, N., Andersson, L., Ismail, A., 2025. Experimental investigation of dust explosions with a focus on black mass in battery recycling. J. Loss Prev. Process. Ind. 94, 105526. https://doi.org/10.1016/j.jlp.2024.105526.

International Organization for Standardization, 2003. Flat Pallets for Intercontinental Materials handling—Principal Dimensions and Tolerances. ISO (ISO 6780:2003) Retrieved from. https://www.iso.org/standard/30524.html.

International Organization for Standardization, 2012. Packaging—Complete, Filled Transport Packages and Unit loads—Dimensions of Rigid Rectangular Packages. ISO (ISO 3394:2012) Retrieved from. https://www.iso.org/standard/50990.html.

Jung, K., Seo, D., Choi, Y., Ko, Y., Kim, C., 2026. Explosion and self-heating hazards of wood pellet dust: a comparative assessment with wood dust and bituminous coal. J. Loss Prev. Process. Ind., 106035 https://doi.org/10.1016/j.jlp.2026.106035.

Li, D., Zhang, Q., Ma, Q., Shen, S., Chen, J., Ren, S., 2016. Influence of built-in obstacles on unconfined vapor cloud explosion. J. Loss Prev. Process. Ind. 43, 449–456. https://doi.org/10.1016/j.jlp.2016.07.007.

Lucas, M., Atanga, G., Hisken, H., Mauri, L., Skjold, T., 2021. Simulating vented hydrogen deflagrations: improved modelling in the CFD tool FLACS-hydrogen. Int. J. Hydrogen Energy 46 (23), 12464–12473. https://doi.org/10.1016/j.ijhydene.2020.09.073.

Lyu, X., Qiao, Y., Yuan, D., Zhang, Z., Zuo, W., Hua, J., et al., 2024. Investigation and CFD simulation of coal dust explosion accident in confined space: a case study of Gaohe Coal Mine Ventilation Air Methane oxidation power plant. Fire Saf. J. 149, 104237. https://doi.org/10.1016/j.firesaf.2024.104237.

Ma, G., Li, J., Abdel-Jawad, M., 2014. Accuracy improvement in evaluation of gas explosion overpressures in congestions with safety gaps. J. Loss Prev. Process. Ind. 32, 358–366. https://doi.org/10.1016/j.jlp.2014.10.007.

Mahesh, S., Narasimhamurthy, V.D., Skjold, T., 2025. Toward fundamental improvements to engineering models for gas explosions in complex geometries by utilizing experimental results in conjunction with highly resolved numerical simulations. Process Saf. Prog. 44 (4), 682–693. https://doi.org/10.1002/prs.70033.

National Fire Protection Association (NFPA), 2023. NFPA 68: Standard on Explosion Protection by Deflagration Venting. NFPA. Retrieved from. https://link.nfpa.org/publications/68.

Pedersen, H.H., Middha, P., 2012. Modelling of vented gas explosions in the CFD tool FLACS. Chem. Eng. Trans. 26, 357–362. https://doi.org/10.3303/CET1226060.

Pinna, F., Zucca, M., Simoncelli, M., Stochino, F., 2025. Explosion venting in dust collectors: a critical review of standards for reduced pressure and reaction force duration. J. Loss Prev. Process. Ind. 97, 105670. https://doi.org/10.1016/j.jlp.2025.105670.

Pinna, F., Zucca, M., Simoncelli, M., Stochino, F., 2026a. A new logarithmic congestion model for vent sizing and reduced pressure prediction in baghouse dust collectors. J. Loss Prev. Process. Ind., 105829 https://doi.org/10.1016/j.jlp.2025.105829.

Pinna, F., Zucca, M., Simoncelli, M., Stochino, F., 2026b. Dust explosions in baghouse dust collectors: a state-of-the-art review. J. Loss Prev. Process. Ind., 105958 https://doi.org/10.1016/j.jlp.2026.105958.

Puttock, J., Walter, F., Chakraborty, D., Raghunath, S., Sathiah, P., 2022. Numerical simulations of gas explosion using Porosity Distributed Resistance approach Part 1: validation against small-scale experiments. J. Loss Prev. Process. Ind. 75, 104659. https://doi.org/10.1016/j.jlp.2021.104659.

Rack Manufacturers Institute, 2023. Ansi MH16.1-2023: design, testing, and utilization of industrial storage racks. MHI. Retrieved July 21, 2026, from. https://www.mhi.org/search?contentType=Standard&industryGroup=RMI.

Ranwaha, N., Yuen, S.C.K., 2016. The effects of blast-induced fragments on cellular materials. Int. J. Impact Eng. 92, 50–65. https://doi.org/10.1016/j.ijimpeng.2015.12.003.

Skjold, T., Arntzen, B.J., Hansen, O.R., Storvik, I.E., Eckhoff, R.K., 2006. Simulation of dust explosions in complex geometries with experimental input from standardized tests. J. Loss Prev. Process. Ind. 19, 210–217. https://doi.org/10.1016/j.jlp.2005.06.005.

Skjold, T., Castellanos, D., Olsen, K.L., Eckhoff, R.K., 2014. Experimental and numerical investigation of constant volume dust and gas explosions in a 3.6-m flame acceleration tube. J. Loss Prev. Process. Ind. 30, 164–176. https://doi.org/10.1016/j.jlp.2014.05.010.

Skjold, T., Faye, A., Bjørnsen, A., van Wingerden, M., Buseth, T., 2026. Silicon dust explosions in ducts and pipes. J. Loss Prev. Process. Ind., 106111 https://doi.org/10.1016/j.jlp.2026.106111.

Su, H., Guo, C., Liu, N., Liang, X., Zhang, X., 2025. Visualization and analysis of mapping knowledge domain in metal dust explosion research. J. Loss Prev. Process. Ind. 98, 105729. https://doi.org/10.1016/j.jlp.2025.105729.

Tamanini, F., 1990. Turbulence effects on dust explosion venting. Plant Oper. Progr. 9 (1), 52–60. https://doi.org/10.1002/prsb.720090111.

Tamanini, F., 1998. The role of turbulence in dust explosions. J. Loss Prev. Process. Ind. 11 (1), 1–10. https://doi.org/10.1016/S0950-4230(97)00026-0.

Tamanini, F., Valiulis, J.V., 1996. Improved guidelines for the sizing of vents in dust explosions. J. Loss Prev. Process. Ind. 9 (1), 105–118. https://doi.org/10.1016/0950-4230(95)00053-4.

Tascón, A., Aguado, P.J., 2015. CFD simulations to study parameters affecting dust explosion venting in silos. Powder Technol. 272, 132–141. https://doi.org/10.1016/j.powtec.2014.11.031.

Tascón, A., Aguado, P.J., 2017. Simulations of vented dust explosions in a 5 m3 vessel. Powder Technol. 321, 409–418. https://doi.org/10.1016/j.powtec.2017.08.047.

Varela, A., Arbizu-Milagro, J., Tascón, A., 2023. Application of factorial analysis to the study of vented dust explosions in large biomass storage silos. Fire 6 (6), 226. https://doi.org/10.3390/fire6060226.

Vyazmina, E., Jallais, S., 2015. Validation and recommendations for CFD and engineering modeling of hydrogen vented explosions: effects of concentration, obstruction and vent area. In: Proceedings of the 6th International Conference on Hydrogen Safety (ICHS 2015), Yokohama, Japan. Paper 123. https://hysafe.info/ichs2015/images/papers/123.pdf.

Vyazmina, E., Jallais, S., 2016. Validation and recommendations for FLACS CFD and engineering approaches to model hydrogen vented explosions: effects of concentration, obstruction vent area and ignition position. Int. J. Hydrogen Energy 41 (33), 15101–15109. https://doi.org/10.1016/j.ijhydene.2016.05.189.

Wang, F., Peng, Y., He, J., Yang, L., 2026. Experimental study on the synergistic inhibition of methane/coal dust explosion by $CO_2/K_2C_2O_4{\cdot}H_2O$. J. Loss Prev. Process. Ind. 100, 105900. https://doi.org/10.1016/j.jlp.2025.105900.

Wang, L., Liu, Z., Zhang, J., Du, Z., Bao, S., Zhang, Z., Li, C., Yuan, C., 2025. Experimental study on the influence of three typical surfactants on the explosion characteristics of coal dust clouds. J. Loss Prev. Process. Ind. 98, 105716. https://doi.org/10.1016/j.jlp.2025.105716.

Wang, Q., Luo, X., Li, Q., Rui, S., Wang, C., Zhang, A., 2022. Explosion venting of hydrogen-air mixture in an obstructed rectangular tube. Fuel 310, 122473. https://doi.org/10.1016/j.fuel.2021.122473.

Yang, K., Liu, W., Ren, J., Li, S., Zhao, Y., Hu, Q., Pang, L., 2020. Effects of multiple annular obstacles on flame propagation of local corn starch dust in a vertical pipe. J. Loss Prev. Process. Ind. 64, 104077. https://doi.org/10.1016/j.jlp.2020.104077.

Yuan, Z., Khakzad, N., Khan, F., Amyotte, P., 2015. Dust explosions: a threat to the process industries. Process Saf. Environ. Prot. 98, 57–71. https://doi.org/10.1016/j.psep.2015.06.008.

Zalosh, R., 2007. New dust explosion venting design requirements for turbulent operating conditions. J. Loss Prev. Process. Ind. 20 (4–6), 530–535. https://doi.org/10.1016/j.jlp.2007.04.038.

Zhang, J., Yuan, Q., Meng, F., Zhang, H., Ding, S., Chen, H., Amyotte, P., Li, C., Yuan, C., 2024. Experimental study and numerical simulation of the combustion characteristics of dust clouds in vertical pipelines underneath unilateral obstacles. J. Loss Prev. Process. Ind. 87, 105212. https://doi.org/10.1016/j.jlp.2023.105212.